Finlet rails for the reduction of the trailing-edge noise

Fiscaletti, Daniele; Pereira, Lourenco Tercio Lima; Ragni, Daniele

DOI
10.1016/j.jsv.2023.118072

Publication date
2024

Document Version
Final published version

Published in
Journal of Sound and Vibration

Journal of Sound and Vibration 568 (2024) 118072

Contents lists available at ScienceDirect

Journal of Sound and Vibration

journal homepage: www.elsevier.com/locate/jsvi

Finlet rails for the reduction of the trailing-edge noise

Daniele Fiscaletti *, Lourenco Tercio Lima Pereira, Daniele Ragni

Department of Flow Physics and Technology, Faculty of Aerospace Engineering, Delft University of Technology, Kluyverweg 1, 2629 HS, Delft, The Netherlands

ARTICLE INFO

Keywords:
Trailing-edge noise
Finlet rails
Particle image velocimetry

ABSTRACT

The present study focuses on the application of finlet rails as a passive technique of flow control to mitigate trailing-edge noise. Finlet rails are small cylinders whose axes are aligned along the streamwise direction, transversally positioned with respect to the trailing edge. In the first part of this study, the effects of finlet geometry on the aeroacoustic emission of a NACA $63_3 - 018$ airfoil are investigated using an array of microphones. It is observed that reducing the transversal spacing of finlet rails leads to increasing the maximum noise reduction, found to be of 4 decibels at relatively low frequencies. An optimum for the height of the finlets was determined, equivalent to $1.6\delta^*$, where δ^* is the displacement thickness of the boundary layer. With the aim of unveiling the underlying physical mechanism for finlet rails, PIV at high spatial resolution is applied around the surface treatment. It is found that the turbulence energy is lifted-up and moved away from the scattering edge, which attenuates the wall-pressure fluctuations. The observed attenuation of the wall-pressure fluctuations occurs at the energy-containing scales, which is an important difference with finlet fences. In the region underneath the finlet rails, the transversal size of the energetic structures diminishes when the surface treatment is applied. The combination of the lift-up of the turbulence structures, that reduces the wall-pressure fluctuations, with the smaller turbulence scales is responsible for the noise reduction observed for finlet rails.

1. Introduction

The sudden balancing of the pressure difference between suction and pressure sides at the trailing edge of an airfoil under turbulent flow conditions scatters acoustic waves in the form of turbulent-boundary-layer trailing-edge noise (TBL-TE noise) [1,2].

TBL-TE noise is the main source of aeroacoustic noise from wind turbines [3]. In the field of rotorcraft and urban air mobility, TBL-TE noise constitutes a significant contributor to the emitted broadband noise [4,5]. With the aim of attenuating the TBL-TE noise, several passive strategies were recently investigated, including trailing-edge brushes [6], trailing-edge serrations [7–9], porous materials [10,11], streamwise finlets [12–14], and shallow dimples [15]. Lee and co-authors [16] recently provided a comprehensive review on the problem of TBL-TE and on the mitigation strategies that have been proposed.

Trailing-edge serrations are add-ons that are retrofitted to wind-turbine blades with the aim of modifying the straight geometry of the trailing edge. Studies aimed at extending trailing-edge serrations to rotorcrafts were also performed, recently [17]. Trailing-edge serrations reduce the noise at relatively low frequencies, often accompanied by a noise increase at relatively high frequencies [7,18]. The noise reduction mechanism relies on the modification of the scattering process by introducing an angle between the incoming flow direction and the normal to the trailing edge [19]. Once applying trailing edge serrations, the most active region constituting a source of noise remains the serration root. In this region, the most abrupt change of flow impedance is determined, and to

* Corresponding author.
E-mail addresses: d.fiscaletti@tudelft.nl (D. Fiscaletti), l.t.limapereira@tudelft.nl (L.T.L. Pereira), d.ragni@tudelft.nl (D. Ragni).

https://doi.org/10.1016/j.jsv.2023.118072
Received 14 March 2023; Received in revised form 28 September 2023; Accepted 28 September 2023
Available online 30 September 2023

mitigate this problem the scientific community has proposed the use of filaments in the empty space between teeth [9,20]. Sarradj and Geyer [21] were among the first investigators who proposed porous materials to reduce the airfoil self noise by mitigating the unsteady pressure fluctuations imbalance between the pressure side and the suction side at the trailing edge [22]. From the parametric study later performed by Herr et al. [23], several studies have proposed new solutions to exploit the higher noise reduction achieved by increasing the flow permeability at the trailing edge [11,24].

Another route to mitigate airfoil self noise has been inspired by the silent flight of owls. After studying at the microscope the feathers of different species of owls, whose silent flight is for decades a source of inspiration for aeroacousticians [25,26], Clark et al. reproduced the structure of such feathers in a laboratory setting [27]. Canopies of fabric having variable diameter, texture and orientation were suspended above a rough surface to assess their aeroacoustic behavior. These canopies could attenuate both the wall-pressure fluctuations and the far-field noise, with the best performances obtained for canopies oriented along the flow. This suggested that the proper orientation of the flow features prior to the trailing edge could have enhanced the capabilities of a wing to reduce noise. A year later, the same authors tried to replicate the bio-inspired canopy in a form suitable for application to an airfoil [12]. Two different treatment designs were developed, referred to finlet fences and finlet rails, and installed directly upstream of the TE to manipulate the turbulent boundary layer. The application of the finlets could lead to a noise attenuation of up to 9 dB, with a minimal aerodynamic impact.

The pioneering work by Clark et al. [12] was followed by several studies, both experimental and numerical, involving finlet fences for TBL-TE noise reduction. The experiments of Afshari et al. [28] evidenced that to obtain the maximum reduction of the unsteady pressure fluctuations the spacing between the finlets should be of the order of the thickness of the TBL inner layer. The treatment was observed to produce a "channeling effect" on the flow, which increases the energy content of the large scales and enhances the spectral density of the low-frequency wall-pressure fluctuations. Recently, Gstrein et al. [14] applied finlet fences on a NACA 0012 airfoil and found the best noise reduction at mid- to high-frequencies, for an optimal ratio of 0.7 between the fences height and the boundary-layer thickness.

Numerical simulations were also employed to elucidate the underlying mechanism for noise attenuation based on the characteristics of the turbulent flow in the vicinity of the fences. Bodling and Sharma [29] observed that, as a main mechanism for noise reduction, the fences increase the separation distance between the peak of unsteady pressure fluctuations and the scattering edge, thus reducing the noise scattering efficiency. Bodling and Sharma were the first investigators to attribute this to a lift-up of the turbulent eddies away from the wall. Also, the spanwise coherence decreases for length scales larger than the fences spacing, which attenuates TE noise at the mid-frequencies. Shi and Lee [30] found that the surface treatment retards the flow in the finlet channels, with a reduction of the turbulent kinetic energy at the wall. The recent study of Ananthan and Akkermans [31] identifies several interconnected noise reduction mechanisms. Firstly, the finlets 'lift up' the energetic eddies and move them away from the scattering edge. Secondly, the larger wetted area associated with the finlets configuration enhances the dissipative action of the near-wall turbulent structures by wall friction, which dampens the wall-pressure fluctuations. Thirdly, a velocity reduction is observed for the flow exiting the finlets channel towards the TE.

In summary, while the mechanisms of noise reductions behind the employment of finlet fences have been understood, the link between the aerodynamic change of flow features and the acoustic footprint of finlet rails is not clear, yet. According to the study of Clark et al. [12], finlet rails seem to reduce the TBL-TE noise at relatively lower frequencies than finlet fences. Moreover, finlet rails were observed to perform better than finlet fences at high angles of attack, although the channeling flow effect cannot take place in finlet rails due to their different morphology.

The present work aims at elucidating the noise reduction mechanisms of finlet rails for TBL-TE noise. To the purpose, a benchmarked NACA $63_3 - 018$ airfoil was adopted for this study [32], as representative of a typical airfoil for wind turbine applications [33,34]. The study is organized as follows. A detailed description of the applied experimental techniques is presented in Section 2. These techniques involve a microphone array, a wake rake, planar and stereoscopic PIV. Section 3 discusses the results obtained from the experiments, and it is divided into four subsections. Firstly, the effects of finlet geometry on the far-field noise are examined, followed by an analysis of drag coefficient. An investigation into the flow around finlet rails is presented later, and the results section terminates with a discussion of the mechanisms for noise reduction. The most salient findings of the study are then summarized in Section 4.

2. Experimental techniques

The experimental investigations reported in this study were performed in the anechoic vertical wind tunnel (A-Tunnel), at Delft University of Technology (TU Delft) [35]. The benchmarked NACA $63_3 - 018$ from TU Delft, DLR and DTU was employed for the study [24]. The model has a chord c of 0.2 m and a span of 0.4 m. The interchangeable TE inserts made up 20% of the chord. The airfoil was mounted on a 400 mm × 700 mm nozzle opening with two parallel side plates. The transition to turbulence is triggered by a zig-zag tape installed on both sides of the airfoil at 5% of the chord. The width of the zig-zag tape is of 6 mm, the thickness is of 0.5 mm, and the angle is of 70 deg. Tests were conducted at the free-stream velocities $U_1^\infty = 15$, 20, 25, 30 m s^{-1}, corresponding to a Reynolds number based on the airfoil chord of $Re_c \approx 2.0 \times 10^5$, 3.0×10^5, 3.3×10^5, 4×10^5. At these free-stream velocities, the turbulence intensity in the test section was <0.1%. Trailing-edge inserts carrying streamwise rails on both sides of the airfoil model were 3d-printed in resin with a nominal height of the deposition layer of 50 μm. A photo of the airfoil model equipped with a trailing-edge insert with finlet rails and installed inside the A-tunnel is shown in Fig. 1. Having the finlet rails directly on 3d-printed inserts avoids the use of a substrate to connect them to the airfoil surface, which had to be employed in the work of Clark et al. (2017) [12] as well as in later experimental studies on finlet fences [14,28].

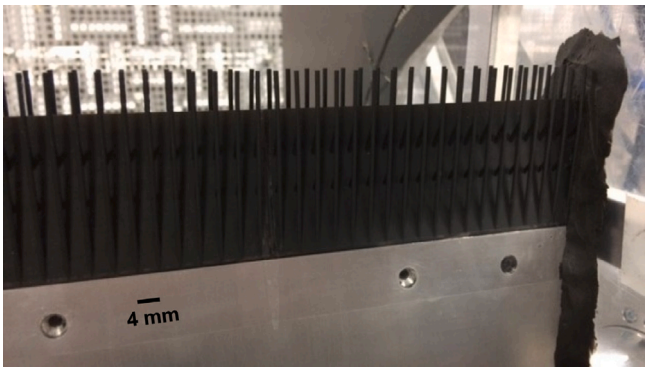

Fig. 1. Photo of the experimental airfoil model of the NACA 63_3-018, with a trailing-edge insert carrying finlet rails. The trailing-edge insert is the black part of the model, and it extends as much as 20% of the chord.

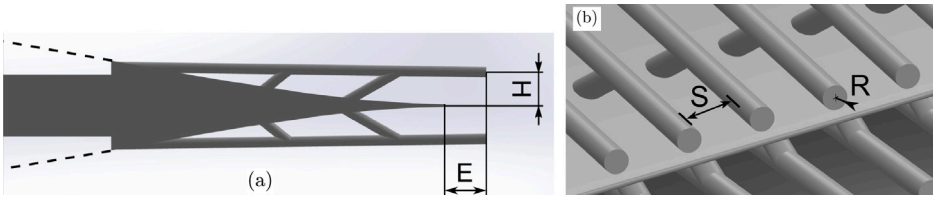

Fig. 2. CAD drawing of a trailing-edge insert used for 3D-printing; (a) view of the x_1x_2 plane, where the dashed lines are the trace of the aluminium part of the model, (b) top view. The different geometrical parameters involved in the design are shown.

Table 1
Transversal spacing (S), height (H), and extension over the trailing edge (E) of the rails on each trailing-edge insert.

	S2p5H3E5	S2p5H4E5	S2p5H4E8	S2p5H4E10	S4H3E5	S4H4E5	S4H4E8	S4H4E10	S4H5E10
Spacing (mm)	2.5	2.5	2.5	2.5	4.0	4.0	4.0	4.0	4.0
Height (mm)	3.0	4.0	4.0	4.0	3.0	4.0	4.0	4.0	5.0
Extension (mm)	5.0	5.0	8.0	10.0	5.0	5.0	8.0	10.0	10.0

In Fig. 2(a), a CAD drawing of a trailing-edge insert is presented, where the blunt step that is visible on the left side is fitted into the aluminium part of the airfoil model, as shown in Fig. 1. The figure shows the different geometrical parameters involved in the design of the surface treatment. Nine inserts carrying rails of different geometries were experimentally investigated. While the radius (R) of the rails as well as their streamwise positioning were kept constant throughout the experimental campaign, their transversal spacing (S), height (H) and extension past the trailing edge (E) were varied from insert to insert. The radius of the rails was of R = 0.625 mm, and their streamwise positioning was at 80% of the airfoil chord from the leading edge, thus covering the full streamwise extent of the insert. In Table 1, the geometric parameters of the finlet rails on the different inserts under analysis are summarized.

An assessment of the trailing-edge noise generated by the different inserts was performed through an array of microphones, while a traversing wake rake was used to estimate the drag coefficient. A schematic of the experimental setup is shown in Fig. 3. Although in this schematic the array of microphones and the wake rake are drawn as if simultaneously present, the measurements of far-field noise are carried out without the wake rake installed. A $x_1x_2x_3$ Cartesian system is introduced here, centered in the mid span of the trailing edge of the airfoil, and oriented such that the x_1 axis is in the streamwise direction, and the x_3-axis is in the spanwise direction, as shown in Fig. 3. The array of microphones is constituted of 64 G.R.A.S. 40PH microphones having a flat frequency response (±1 dB) within a frequency range from 10 Hz to 20 kHz, with a maximum output of 135 dB, ref. 2×10^5 Pa. The array is arranged in an optimized multi-arm spiral configuration, with the array plane placed parallel to the x_1x_3 plane. The central microphone has coordinate $(x_1, x_2, x_3) = (0.45c, 5c, 0)$. The sampling time per case was 20 s with a sampling frequency of 51.2 kHz. The Cross-Spectral Matrix (CSM) of the signal was obtained by averaging the CSMs constructed from snapshots of the time-domain signal, using a Hanning windowing function (Welch's method). Each snapshot contained 5120 samples, yielding a final frequency resolution of 10 Hz. The $5c \times 5c$ scan plane was defined with a distance of 10 mm between adjacent scan grid points, centered at the origin of the coordinate system. Conventional Frequency-Domain Beamforming (CFDBF) was first applied to reconstruct the acoustic source map. Then, in order to accurately extract only the TBL-TE noise from the source map, the source power integration (SPI) method was applied using a region of integration (ROI) centered with the trailing-edge mid-span and covering half of the span and 50% chord, $(\Delta x_1, \Delta x_2, \Delta x_3) = (0.5c, 0, 1.0c)$. The span-wise limit is selected in order to prevent spurious corner sources from affecting the measurements. The SPLs below −6 dB relative to the maximum SPL in the CFDBF source map at each frequency were

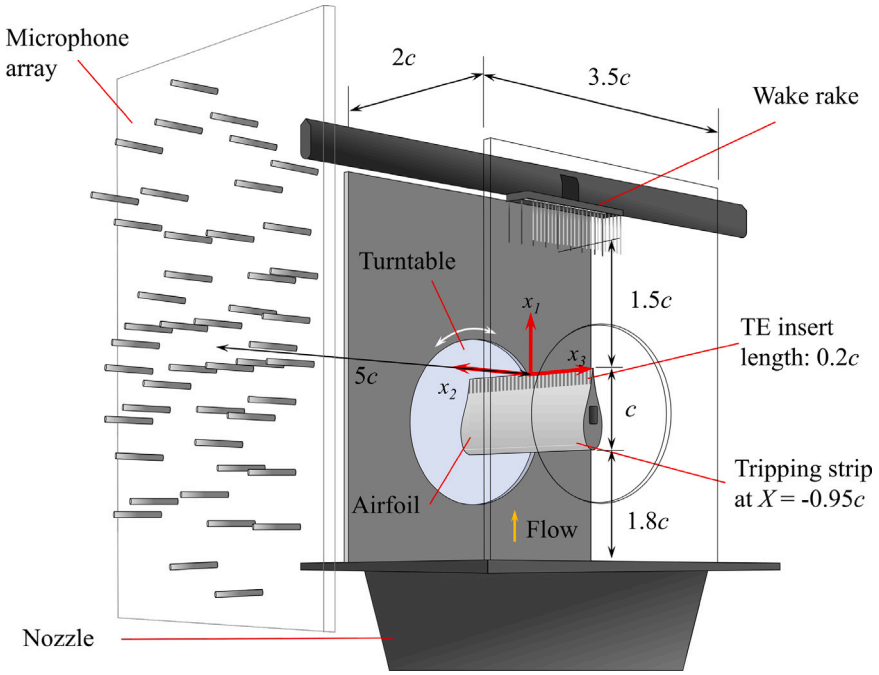

Fig. 3. Schematic of the wind-tunnel test set-up, measurement devices, and coordinate system.

rejected from the integration. Having obtained the source power, the SPLs were calculated using the reference distance of 1 m. The uncertainty in the reconstructed spectra of pressure signals from the array of microphones and with the described post-processing procedure is of ±1 dB [32].

The drag was estimated using a traversing wake rake of Pitot probes, to integrate the total pressure loss and compute the drag coefficients c_d of the NACA 63_3-018 airfoil model with different TE inserts. The wake rake consisted of 50 and 12 total and static pressure probes, respectively. The total pressure probes spanned a distance of $1.1c$. The spacing of the total pressure probes was of 3 mm, while the static pressure probes were distributed with a spacing of 12 mm. Pressure data were acquired by *HoneyWell TruStability* differential pressure transducers. The nominal accuracy of the transducers was of 3 Pa, the sampling frequency was of each individual sensor was about 20 Hz for an acquisition time of 20 s. The wake rake was positioned at approximately $x = 1.5c$. The center of the wake rake was adjusted according to the geometrical angle-of-attack in such a way that the momentum-deficit region in the wake was well contained within the wake-rake span. The drag is then computed by the following integral across the wake (see Barlow et al. [36], Houghton and Carpenter [37] and Russo [38]):

$$c_d = \frac{2}{c}\int_{\text{wake}} \sqrt{c_{p,t}-c_{p,s}}\left(1-\sqrt{c_{p,t}}\right)\mathrm{d}y. \tag{1}$$

where $c_{p,t}$ is the total pressure coefficient and $c_{p,s}$ is the static pressure coefficients. To attenuate the experimental error in the estimate of the coefficient of drag c_d, an asymmetric Gaussian fitting was applied to the profile of the experimental values of $c_{p,t}$ and $c_{p,s}$, and the analytical equation was used to compute Eq. (1). The aforementioned nominal accuracy of 3 Pa of the pressure transducers is associated with an uncertainty on the measurement of the coefficient of drag of $5.685\cdot10^{-5}$, estimated from the theory of uncertainty propagation [39]. This led to a maximum relative uncertainty of less than 0.3%.

Boundary-layer profiles close to the trailing-edge region were measured to determine the flow properties which are used for scaling and comparison of acoustic spectra. The measurements were performed with a hot-wire probe conditioned with a constant-temperature circuit (CTA). A single-sensor miniature wire probe model 55P15 (boundary-layer type) from Dantec Dynamics was used. The sensitive wire is made of platinum-plated tungsten having a length of 1.25 mm and a diameter of 5 μm. The probe was positioned at $x_1 = -0.02c$ and $x_3 = -0.3c$ and was traversed in the $-x_2$ direction using a Zaber LRQXXXHL-DE51T3 traverse controller. The temperature control and the data acquisition were accomplished via a TSI IFA-300 CTA module and a NI-9234 data acquisition card respectively. Data was collected in 71 different points in the $-x_2$ direction, with more data points collected near the wall. Each acquisition was of 2 s at a sampling frequency of 51.2 kHz. The calibration of the probe was carried out using forth-order polynomial curve fitting of the output voltages, with data from 17 speed-voltage data points logarithmically spaced between the lowest and the highest free-stream flow speed. The calibration speeds were measured upstream of the airfoil, i.e. close to the nozzle lip, and the velocity information was taken from a Pitot tube installed near the hot-wire probe. Having obtained the velocity profiles, the edge velocity U_e as well as other properties of the turbulent boundary layer, such as the displacement thickness δ^*, momentum thickness θ, and the boundary-layer thickness δ_{99}, were extracted using an iterative method that was found to work robustly with

Table 2
Boundary-layer properties measured at the trailing edge of the airfoil at $\alpha = 0$ deg, values shown in the work of Luesutthiviboon et al. [32].

U_1^∞ (m s^{-1})	Re_c (–)	δ_{99} (mm)	δ^* (mm)	θ (mm)	U_e (m s^{-1})	u_τ (m s^{-1})	Π (–)
15	2×10^5	9.2	2.23	1.33	14.2	0.52	1.7
20	3×10^5	9.1	2.40	1.36	18.8	0.62	2.3
30	4×10^5	8.9	2.54	1.37	28.1	0.81	3.0

Table 3
Technical specifications of the PIV measurements.

	Field of view (mm)	Window size (px)	Window overlap (%)	Vector spacing (μm)	Δt (μs)	px mm^{-1} (–)	ϵ_i (m s^{-1})
Planar PIV	27 × 23	16 × 16	75	40	10	99.60	0.3
Stereo PIV	91 × 89	32 × 32	75	271	25	29.48	0.4

various experimental and simulated turbulent boundary layers subjected to pressure gradient [40]. The properties of the turbulent boundary layer measured at the trailing edge of the airfoil at $\alpha = 0$ deg are presented in Table 2.

A characterization of the turbulent flow around the finlet rails was performed with particle image velocimetry (PIV). Two experimental campaigns were conducted, one of planar PIV, where velocity fields were measured on the plane x_1x_2, and one of stereoscopic PIV, where velocity fields were measured on the plane x_2x_3, in both cases perpendicularly to the airfoil plane. In the planar PIV campaign two cameras were used, in such a way to investigate the effects of the passive flow treatment both on the turbulent boundary layer and on the wake. The vector spacing for planar PIV was of 40 μm, obtained with a 75% overlapping of correlation windows of 16 × 16 pixels. Adrian & Westerweel suggest a universal uncertainty of 0.1 pixel units for planar-PIV velocity measurements [41]. A conservative estimate of 0.3 pixel units was adopted here, which is expected to be considered for regions characterized by intense shear according to Sciacchitano (2019) and to Shan et al. (2014) [42,43]. An uncertainty of 0.3 pixel units translates to an uncertainty on the instantaneous velocity (ϵ_i) of 0.3 m s^{-1}. Stereoscopic PIV was performed on two x_2x_3 planes, at two different downstream positions, i.e. at the trailing edge ($x_1 = 0$) and at 5 mm downstream from the trailing edge ($x_1 = 5$ mm). The vector spacing for stereoscopic PIV was of 271 μm, obtained with a 75% overlapping of correlation windows of 32 × 32 pixels. An uncertainty of the pixel displacement of 0.3 pixel translates here to an uncertainty on the instantaneous velocity of 0.4 m s^{-1}. A summary of the technical specifications of both the planar PIV and the stereoscopic PIV measurement is presented in Table 3. In each PIV campaign, the thickness of the light sheet was estimated to be lower than 1 mm. The flow was seeded through DEHS droplets (Di(2-ethylhexyl) sebacate, sebacic acid), generated from a Laskin nozzle. The droplets were injected upstream with respect to the settling chamber, so to avoid perturbing the turbulent flow at the measurement section. A total of 3.600 image pairs were acquired for each measurement point.

3. Results

3.1. Far-field noise

The analysis of the results starts with the acoustic measurements from the microphone array. Fig. 4 shows the comparisons between the acoustic source maps from the baseline case (Fig. 4a to c) and the one obtained with the rail insert S2p5H4E5 (Fig. 4d to f), taken as the reference insert for the remainder aerodynamic analysis. These results are obtained for zero angle-of-attack and at the free-stream velocity $U_1^\infty = 30$ m s^{-1}, corresponding to a Reynolds number based on the chord of $Re_c = 4 \times 10^5$. The maps clearly show the source of airfoil self noise at the airfoil trailing edge. At the two lowest frequencies ($f = 1000$ Hz and 2000 Hz), the rail insert is able to reduce the levels by as much as −3 dB. At the highest frequency ($f = 3000$ Hz), however, the acoustic noise increases with respect to the baseline case. This behavior, i.e. reduction of noise in low-to-mid frequencies and increase of noise at high frequencies, is observed for all the inserts tested.

The noise attenuation spectrum integrated from the maps for the different inserts geometries under analysis are shown in Fig. 5. These results were obtained for a free-stream velocity of $U_1^\infty = 30$ m s^{-1}, the same as for Fig. 4. A negative delta sound pressure level ($\Delta SPL < 0$) means a noise reduction with respect to the baseline configuration. Overall, it can be observed that rails are capable of attenuating the trailing-edge noise at frequencies lower than 2.0 kHz. A penalty is however paid at high frequencies. In Fig. 5(a), the spacing between the rails is varied from $S = 2.5$ mm to $S = 4.0$ mm, while both the height and the extension are kept constant, and respectively equal to $H = 3$ mm and $E = 4$ mm. Decreasing the spacing between the rails leads to an improvement of the maximum noise attenuation, while the high-frequency range appears to be mostly unaffected. In Fig. 5(b), the aeroacoustic effect of rails height is assessed for a spacing of $S = 2.5$ mm. Increasing the height appears to penalize both the maximum noise attenuation at low frequency and the high-frequency noise increase. Among all the inserts that were investigated, the insert S2p5H4E5 produces the maximum noise attenuation, approximately 4 dB, which is obtained at a frequency of 1.1 kHz, equivalent to a Strouhal number based on the displacement thickness of $St_{\delta^*} = 0.093$. This Strouhal number is comparable to the one observed for other technologies such as serrations [32]. Analogous results as those reported in Fig. 5(b) are obtained for $S = 4$ mm, although not shown here. Despite these observations suggest that increasing the height improves the noise attenuation performances, a different behavior is found when raising the height from $H = 4$ mm to $H = 5$ mm. Fig. 5(c) evidences that, while the maximum noise reduction does not

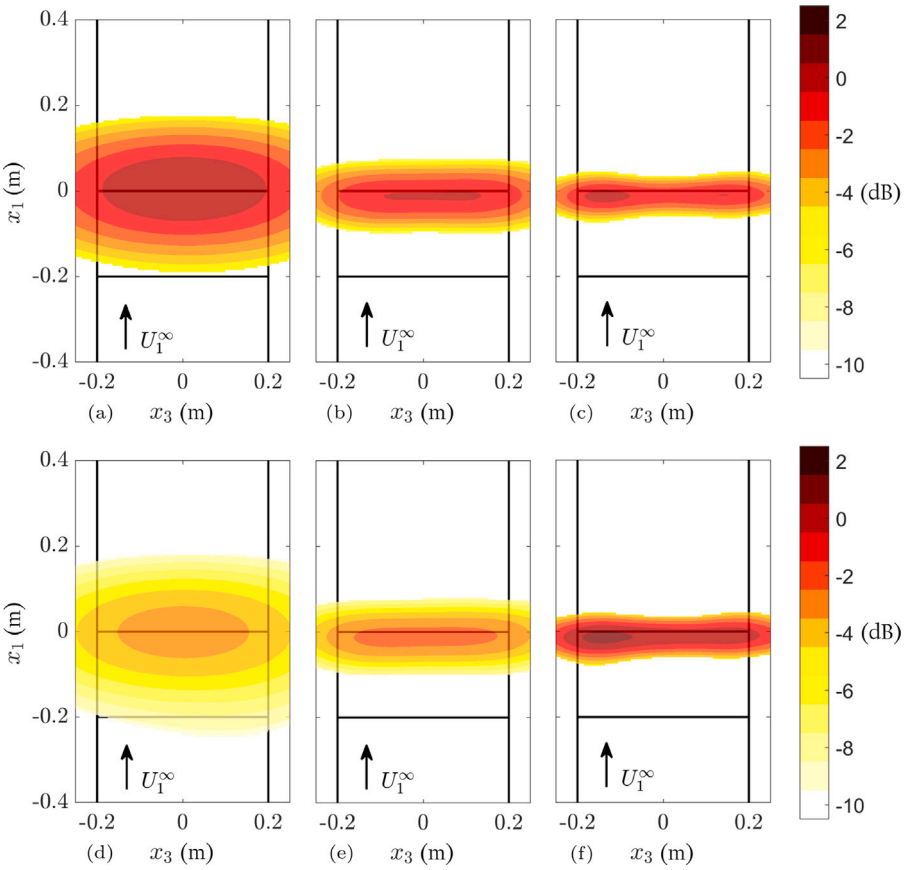

Fig. 4. Comparison between the acoustic source maps obtained at three different frequencies, i.e. (a,d) 1000 Hz, (b,e) 2000, and (c,f) 3000 Hz, at the free-stream velocity of U_1^∞ = 30 m s^{-1}, and for a constant angle-of-attack of $\alpha = 0$ deg. Panels a–c show the maps for the baseline configuration, panels d–f show the maps for the insert S2p5H4E5.

vary, the high-frequency penalty grows, which results in a general deterioration of the performances. It appears therefore that an optimum value exists for the height of rails, beyond which the aeroacoustic behavior of the passive treatment worsens, which can be related with the thickness of the turbulent boundary layer. The described behavior is consistent with the observations of Clark et al. (2017) Clark et al. [12], who also found a high-frequency noise increase when doubling the rails height, i.e. from 4 mm to 8 mm. Finally, the extension of the rails over the trailing edge is assessed in Fig. 5(d). It is found that augmenting the extension beyond $E = 5$ mm reduces the aeroacoustic benefits.

The aeroacoustic performances of the three insert geometries producing the largest levels of noise mitigation at zero angle-of-attack are assessed for effective angles-of-attack equal to 2 deg, 4 deg, and 6.1 deg. The results obtained at $\alpha_{eff} = 0$ are also reported in Fig. 6(a) for reference. Overall, increasing the angle-of-attack deteriorates the acoustic performances of each of the three inserts examined here. This applies both to the high-frequency penalty as well as to the low-frequency noise mitigation region. The insert that suffers the most the deviations from the zero angle-of-attack is S2p5H4E5. The latter is particularly evident for the high-frequency penalty, which grows significantly when moving from $\alpha_{eff} = 0$ deg to $\alpha_{eff} = 4$ deg. The maximum noise reduction decreases with the angle-of-attack, declining from 4 dB to 2 dB. However, S2p5H4E5 remains the insert producing the maximum noise reduction regardless of the angle-of-attack. A decrease in the height of the finlet rails seems to produce a more robust behavior to variations of the angle-of-attack, which is what we can observe when comparing S2p5H4E5 with S2p5H3E5. On the other hand, from this analysis it appears that the least sensitive insert to variations of the angle-of-attack is S4H3E5.

3.2. Aerodynamic performance

In the previous section we found that finlet rails can lead to a noise reduction of up to 4 dB in the low- to mid-frequency range. To assess the feasibility of this noise-attenuation technique for engineering applications, it is of interest to determine how and to what extent the application of the finlet rails affects the aerodynamics. Clark et al. [12] found no measurable effects on the lift coefficient, but the drag coefficient was reported to increase. As follows, we present the results of the wake survey to assess the effects of finlet rails on the drag coefficient. Further details of this analysis are given in Section 2. The experimental assessment

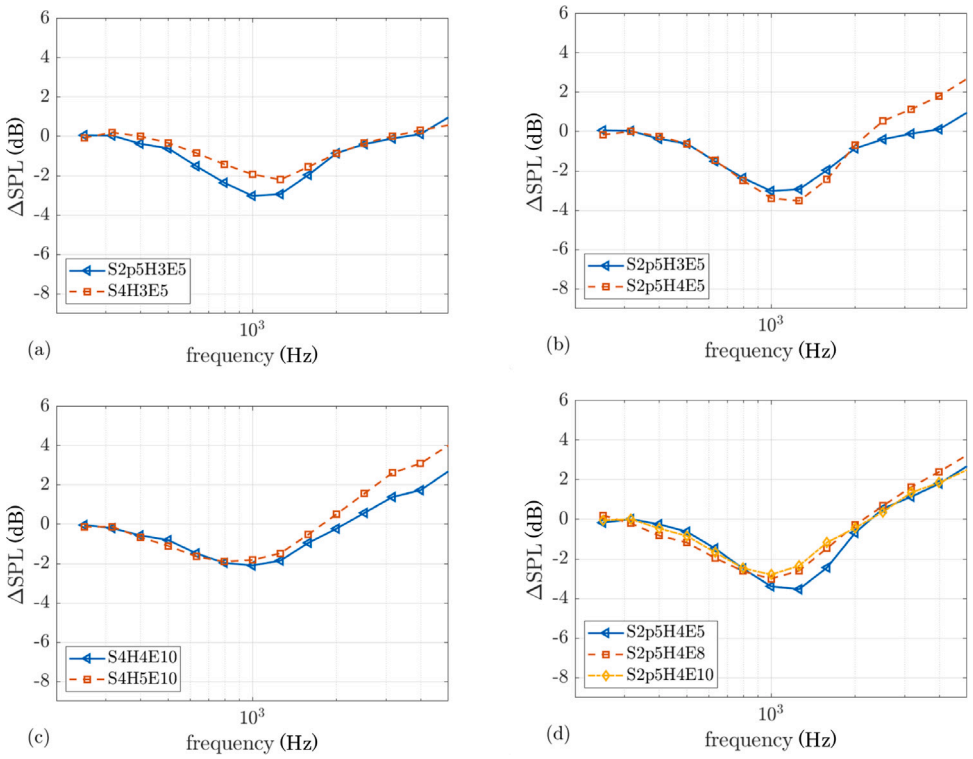

Fig. 5. Noise attenuation in 1/3-octave band obtained from trailing-edge inserts carrying finlet rails as compared with the baseline configuration, at the free-stream velocity of $U_1^\infty = 30$ m s^{-1}, and for a constant angle-of-attack of $\alpha_{eff} = 0$ deg. Specifically, the trailing-edge inserts under investigation are (a) S2p5H3E5 and S4H3E5, (b) S2p5H3E5 and S2p5H4E5, (c) S4H4E10 and S4H5E10, and (d) S2p5H4E5, S2p5H4E8, S2p5H4E10. Therefore, each panel shows the effects of modifying only one geometric parameter for the finlet rails, while keeping the others constant.

Table 4
Percentage increase of the coefficient of drag (c_d) resulting from the application of inserts with finlet rails of different geometries, at three different effective angles of attack (α_{eff}).

α_{eff}	S2p5H3E5	S2p5H4E5	S2p5H4E8	S2p5H4E10	S4H3E5	S4H4E5	S4H4E10	S4H5E10
0 (deg)	12.4%	12.7%	16.6%	16.2%	7.0%	11.5%	12.5%	49.6%
3 (deg)	12.6%	14.7%	19.2%	16.5%	7.3%	12.0%	12.0%	43.1%
6.1 (deg)	13.5%	15.7%	21.1%	18.0%	5.7%	13.1%	11.7%	38.9%

was applied to the trailing-edge inserts reported in Table 1, for varying geometric angle-of-attack α and free-stream velocity U_1^∞. The results obtained for the free-stream velocity of $U_1^\infty = 30$ m s^{-1} as a function of the angle-of-attack are presented in Fig. 7. The coefficient of drag measured for the baseline case, i.e. the untreated airfoil, is also shown in each panel of the figure using black continuous lines and filled circles.

The panels in the top row, namely Fig. 7(a) and (b), show that increasing the spacing between the finlet rails (S ↑) is associated with a decrease of the drag coefficient (c_d ↓). From these two panels, we can also infer that an increase of the rails height (H ↑) is associated with a growth of the drag coefficient (c_d ↑), which can be expected as the treatment enhances the friction surface. This means that the inserts mostly affect the zero-angle-of-attack drag coefficient ($c_{d,o}$), without affecting significantly the pressure drag of the airfoil. However, when raising the rails height up to $H = 5$ mm, a completely different behavior is observed, with an abrupt growth of the drag coefficient, as shown in Fig. 7(f). It is found that, at $\alpha_{eff} = 0$, the insert S4H5E10 produces a 49.5% drag increase with respect to the baseline configuration, which is a much larger percentage than these found for the inserts examined up until here. The figure discussed until here shows the drag coefficients for a selection of inserts. In Table 4, the percentage increase of the drag coefficients for all inserts at zero angle-of-attack is reported.

In summary, the experimental analyses that have been presented so far could quantify the effects of varying the geometric parameters of finlet rails on their aeroacoustic and aerodynamic behavior, when applied on an airfoil model of a NACA $63_3 - 018$. In the remainder of this study, a deeper analysis on the turbulent flow around the finlet rails is carried out to describe the physical mechanism behind the observed noise reduction. This analysis relies on the PIV measurements on the reference insert, the S2p5H4E5, and on its comparison with the baseline case.

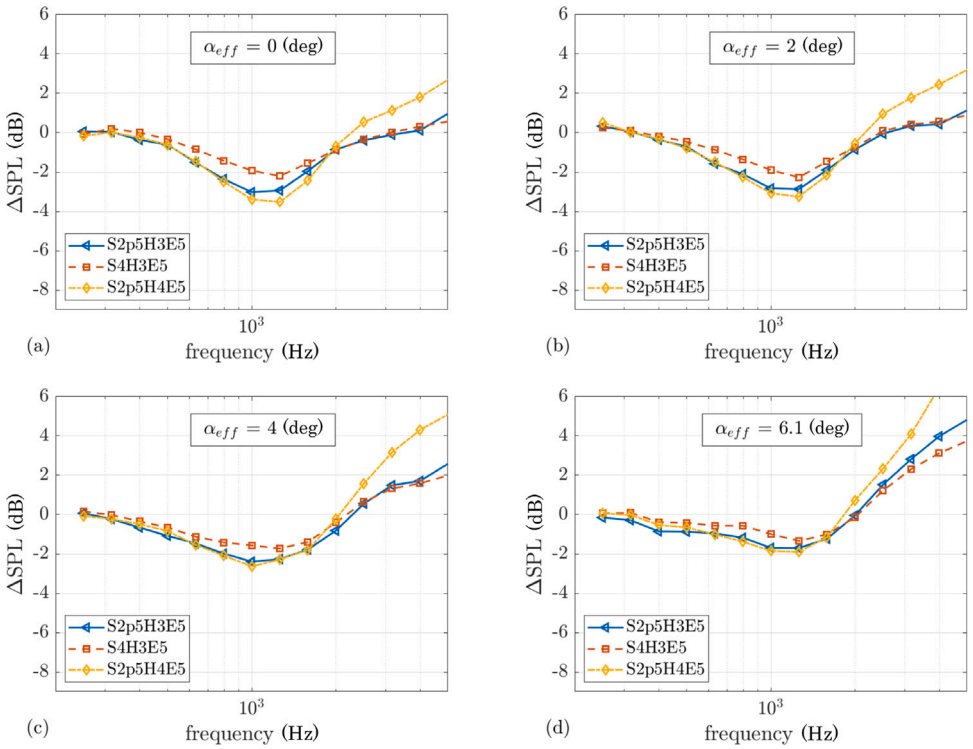

Fig. 6. Noise attenuation in 1/3-octave band obtained from the three inserts S2p5H3E5, S4H3E5 and S2p5H4E5 as compared with the baseline configuration, at the free-stream velocity of U_1^∞ = 30 m s^{-1}. Four effective angles of attack are examined (a) α_{eff} = 0 deg, (b) α_{eff} = 2 deg, (c) α_{eff} = 4 deg, and (d) α_{eff} = 6.1 deg.

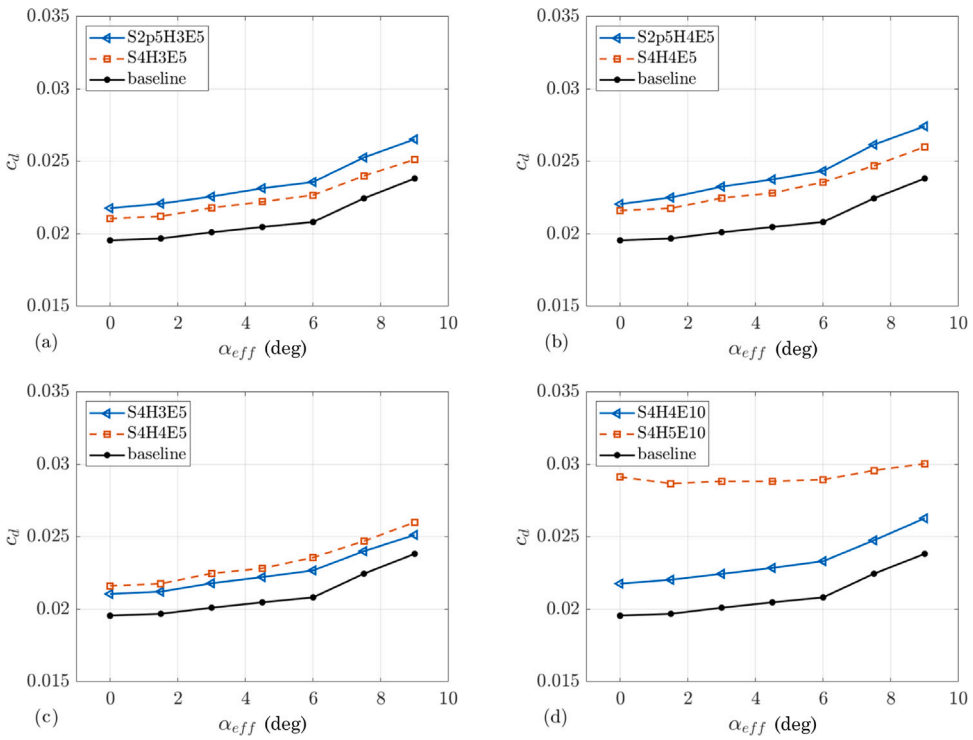

Fig. 7. Effect of the insert geometry on the coefficient of drag for different effective angles-of-attack as estimated from the wake survey through Eq. (1). Specifically, the trailing-edge inserts under investigation are (a) S2p5H3E5 and S4H3E5, (b) S2p5H4E5 and S4H4E5, (c) S4H3E5 and S4H4E5, and (d) S4H4E10 and S4H5E10. The baseline case is also included in each panel.

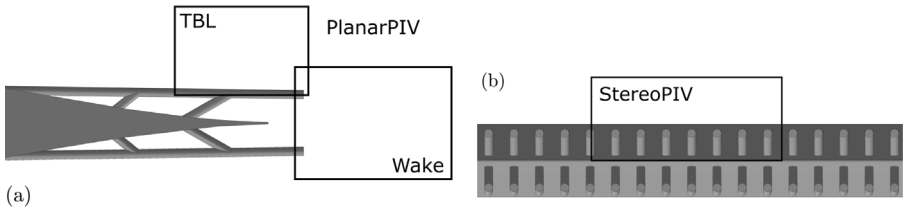

Fig. 8. Schematics showing the fields of view of the two experimental campaigns of PIV; (a) the fields of view on the plane x_1x_2 from the two cameras from planar PIV; (b) the field of view on the plane x_2x_3 from stereoscopic PIV.

3.3. Flow around finlet rails

In this section, the turbulent flow around the finlet rails is described and compared against the flow around the baseline case. Velocity fields from the PIV measurements presented in Section 2 are examined in the following. It is firstly of interest to show the fields of view of the two PIV experimental campaigns. Fig. 8 illustrates the extent of the fields of view and their positions relative to the model. The campaign of planar PIV was conducted using two cameras, one pointing at the turbulent boundary layer above the finlet rails, and another pointing at the wake behind the model, both of them on the plane x_1x_2. The two fields of view from the two cameras are conveniently tagged in the schematic in Fig. 8(a). It is worth highlighting that the light sheet, and thus the measurement plane, passes through one of the finlet rails. In Fig. 8(b), another schematic shows the field of view of the stereoscopic PIV experimental campaign, this on the x_2x_3 plane.

Mean and r.m.s. from the field of view 'Wake' are presented in Fig. 9. The two black regions on the left side of the panels on the right column (b,d) represent the shadowing of the finlet rails. In the top row (a,b), maps of the mean streamwise velocity for the baseline case (a) and for the case with the insert S2p5H4E5 (b) are shown. It can be observed that the velocity deficit behind the baseline model extends over a relatively smaller region and is weaker when compared with the velocity deficit behind the finlet rails. This explains the increase of the coefficient of drag associated with the application of finlet rails, which from Fig. 7(b) can be quantified as 12.7%. The bottom row of panels shows maps of r.m.s. streamwise velocity for the baseline case (Fig. 7c) and for the case with the insert S2p5H4E5 (Fig. 7d). The panel of the baseline case (c) exhibits two regions of relatively high r.m.s. streamwise velocity that are symmetrically organized with respect to the centerline ($x_2 = 0$). These energetic regions are produced by the wall shear from the suction and the pressure sides of the airfoil, and they are characterized by values of r.m.s. streamwise velocity in the range between 2.5 m s^{-1} and 3 m s^{-1}, whose intensity decreases with the downstream location. The panel of the insert S2p5H4E5 presents a similar behavior. However, two smaller regions of even stronger r.m.s. velocity are observed for this case, where r.m.s. values up to 4 m s^{-1} are reached. These regions could be associated either with the shear produced by the walls of the finlet rails or with the shedding of vortices generated by the finlet rails. Their extent along the x_2 direction is of the same order of magnitude as the rails diameter, and they extend in the downstream direction over approximately 15 mm, equivalent to $3E$. It is worth mentioning that in proximity to the insert ($x_1/E < 1$) the PIV measurement is contaminated by the reflections and shadowing from the insert.

Mean and r.m.s. of the streamwise velocity fluctuations calculated from PIV measurements in the field of view 'TBL' are presented in Fig. 10. The black stripes at the bottom of the panels on the right column (b,d) represent the shadowing caused by the finlet rails on the insert. In the top row (a,b), maps of the mean streamwise velocity for the baseline case (a) and for case with the insert S2p5H4E5 (b) are presented. It can be observed that the turbulent boundary layer is thicker for the case with the insert when compared with the baseline case. Therefore, the insert produces an increase of the overall boundary layer thickness, which is quantified later in this section by locating the position of the turbulent/non-turbulent interface. These observations are confirmed when looking at the maps of the r.m.s. streamwise velocity, in the bottom row of Fig. 10. From the baseline case, Fig. 10(c), the shear from the wall produces a region of intense r.m.s. velocity in the bottom left portion of the panel. In this region, values of 3 m s^{-1} are reached for the r.m.s. streamwise velocity. Of relatively smaller size and lower intensity is the region above the rails, where the maximum r.m.s. streamwise velocity is of 2.5 m s^{-1}. In the region above the trailing edge and beyond ($x_1/H > 0$), finlet rails determine a mild but broad increase of the r.m.s. even far from the treatment location, at wall-normal positions up to $x_2/H \approx 3$ (Fig. 10(d)). Again, these features will be confirmed from measurements from stereoscopic PIV.

As previously mentioned, we adopted a rigorous approach to quantify the increase of the boundary-layer thickness and the widening of the wake consequent to the surface treatment. This consists in estimating the average position of the turbulent/non-turbulent interface (TNTI) [44,45], and in assessing its shift in consequence of the finlet rails. In the present study, a methodology similar to that proposed by Chauhan et al. [46] was applied. This is based on a threshold applied to the local parameter k over a 3×3 grid. The parameter k is defined as

$$k = 100 \times \frac{1}{9(U_1^{\infty})^2} \sum_{i,j=-1}^{1} [(U_1(x_1^* + i, x_2^* + j) - U_1^{\infty})^2 + (U_2(x_1^* + i, x_2^* + j))^2], \tag{2}$$

and approximates the turbulent kinetic energy in the free-field region in a point of the domain [46]. The choice of a threshold value was made based on an analysis of the extent of the turbulent region, as a function of a variable threshold obtained from the

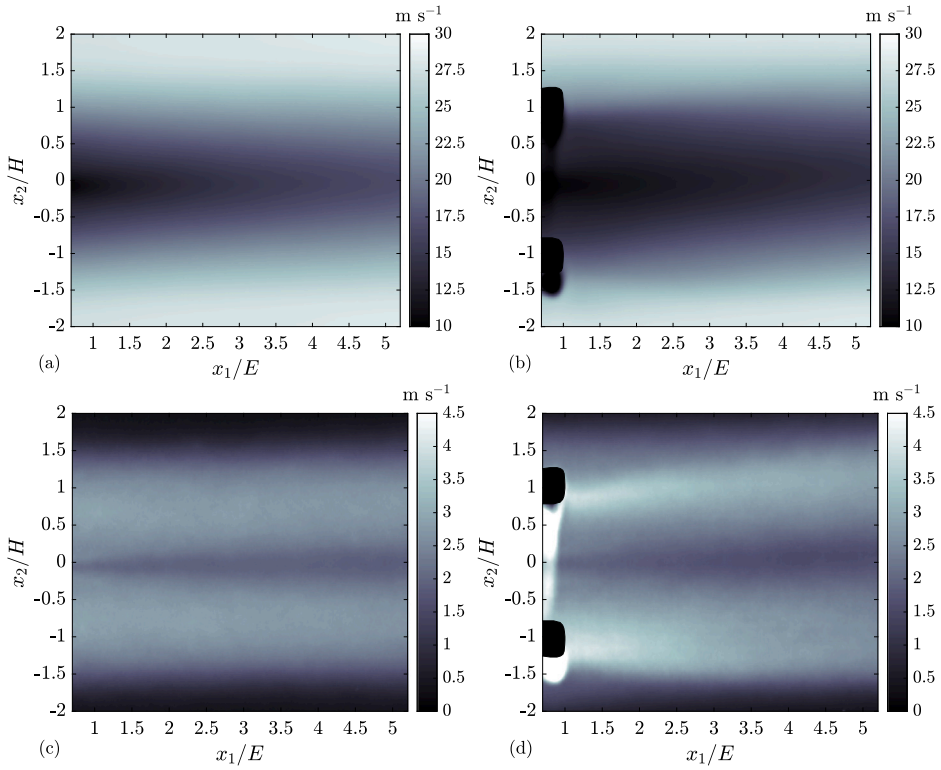

Fig. 9. Mean and r.m.s. streamwise velocity from planar PIV applied to the field of view tagged as 'Wake' in Fig. 8. (a,b) Mean streamwise velocity, $\overline{U_1}$, for (a) the baseline case and (b) the case with insert S2p5H4E5; (c,d) r.m.s. streamwise velocity, $U^{rms}{}_1$, for (c) the baseline case and (d) the case with insert S2p5H4E5.

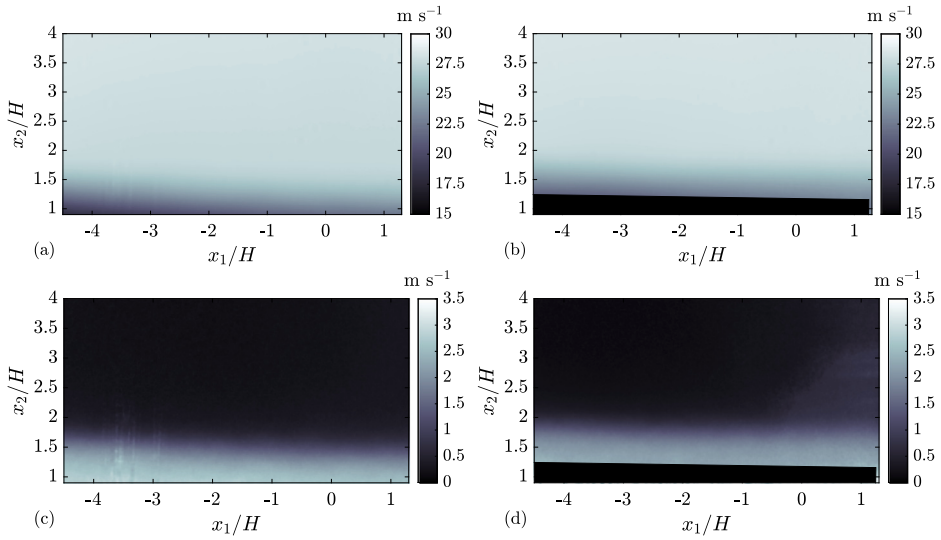

Fig. 10. Mean and r.m.s. streamwise velocity from planar PIV applied to the field of view tagged as 'TBL' in Fig. 8. (a,b) Mean streamwise velocity, $\overline{U_1}$, for (a) the baseline case and (b) the case with insert S2p5H4E5; (c,d) r.m.s. streamwise velocity, $U^{rms}{}_1$, for (c) the baseline case and (d) the case with insert S2p5H4E5.

product between k and a variable constant, analogous to Attili, Cristancho and Bisetti [47] (see their Appendix). The value that gave the most stable extent of the turbulent region was taken as the threshold beyond which the flow was considered turbulent. The application of this procedure to each realization produced a local estimate for the TNTI. The average positions of the TNTI for both fields of view are reported in Fig. 11. Fig. 11(a) shows the positions of the TNTIs (top and bottom ones) for the 'Wake' field

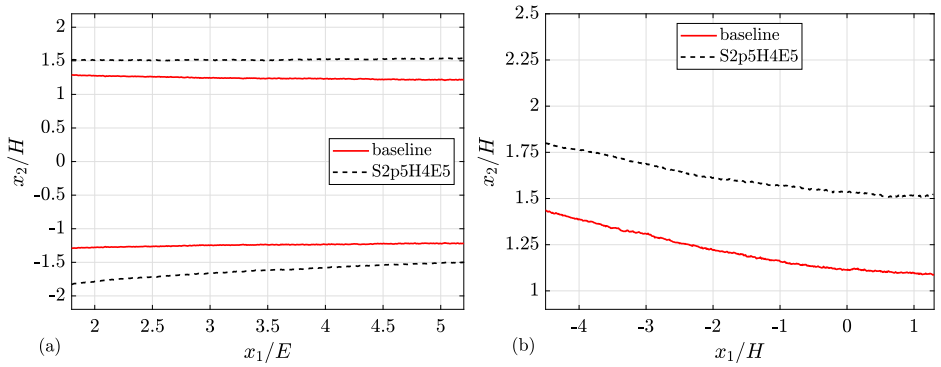

Fig. 11. Turbulent/non-turbulent interfaces (TNTIs) calculated following the procedure of [46], from velocity fields (a) from the field of view denominated 'Wake', and (b) from the field of view denominated 'TBL' (Fig. 8).

of view, both for the baseline case (continuous line) and for the case with finlet rails (dashed line). It can be observed that the application of the insert with finlets makes the wake wider. From our analysis, at $x_1/E = 2$ the wake becomes approximately $0.7H$ wider after the application of the finlets, while the difference between the two wakes reduces to $0.6H$ at the downstream locations $x_1/E = 4.5-5$. This determines the drag increase of 12.7% that was measured with the wake rake (Section 3.2). Fig. 11(b) shows the position of the TNTI for the 'TBL' field of view. Consistent to what discussed previously, the finlet rails determine an upwards shift of the TNTI compared with the baseline case by approximately $0.35-0.40H$. The increase in the thickness of the turbulent boundary layer remains almost constant across the downstream positions under analysis. It is worth stressing here that the discussion on the wake and on the turbulent boundary layer obtained from the analysis of Figs. 9 and 10 are related to a plane passing through a finlet rail, as mentioned at the beginning of the subsection. A thinner boundary layer and a more narrow wake are expected for planes perpendicular to the TE and located in between rails.

Fig. 12 shows mean and r.m.s. on the x_2x_3 plane passing through the trailing edge ($x_1 = 0$). It was decided not to mask the measurements associated with the finlets being cut off by the measurement plane because their footprints can be detected by the streamwise velocity being approximately zero in those regions (dark blue). The panels in the top row (a,b) show maps of mean streamwise velocity for the baseline case (a) and for case with the insert S2p5H4E5 (b). From comparing the two maps in the top row of the figure, it can be observed that the rails determine a strong velocity deficit in the region underneath their footprints. For the baseline case, the streamwise velocity distribution along the x_2 direction exhibits a relatively gradual increase from the low values at the wall up U_1^∞. On the other hand, the finlet rails determine a much steeper transition, particularly above the region where the finlet rails are located. In the panels in the bottom row (c,d), maps of r.m.s. streamwise velocity are presented, for the baseline case (c) and for the case with the insert S2p5H4E5 (d). From the baseline case, the turbulent boundary layer produces a relatively larger energy content that appears uniform in the transversal direction. It is however worth noting that the maximum in the r.m.s. velocity along the wall-normal direction does not occur in proximity to the wall, but at a higher wall-normal location. With finlets we observe how the region underneath the finlets is characterized by a lower level of turbulent energy compared with the baseline case. Above the regions that can be identified as finlets footprints, curved layers of intense r.m.s. velocity can be observed. Higher levels of uncertainty are associated with these measured values of r.m.s. velocity, which are caused by intense reflections from the insert model in the PIV images. However, r.m.s. velocities of approximately 4 m s^{-1} were also found from planar PIV measurements in the wake behind the finlet rails, in Fig. 9, which gives support to these values measured with stereoscopic PIV.

Fig. 13 presents the mean and r.m.s. from stereoscopic PIV on the x_2x_3 plane, at 5 mm distance from the trailing edge in the downstream direction, therefore at the edge of the finlet rails. It is worth stressing that measurement plane is purely in the wake. Here, therefore, the PIV plane does not intersect the finlets, which results in no shadowing and no reflections. From the maps of the mean streamwise velocity for the baseline case (a) and for case with the insert S2p5H4E5 (b), it is again evident how the application of the finlet rails leads to a region of momentum deficit that covers the whole space underneath the finlets themselves. This is followed by a sharp recovery of the flow velocity, which rapidly increases to U_1^∞ above the finlets. Moreover, the momentum deficit underneath the treatment generates a marked attenuation of the energy content in the flow, as can be seen when comparing the r.m.s. streamwise velocities in the cases without and with finlets, respectively in Fig. 13(c) and (d). Above the region in the wake of the finlet rails, the r.m.s. streamwise velocity exhibits a marked growth, and values between 3.5 and 4 m s^{-1} are measured, in this case without any significant reflections afflicting the image quality and therefore the measurements. The periodically reoccurring protrusions having a transversal spacing of the same order of magnitude as their characteristic size (in this case their diameter $2R = 1.25$ mm) produce a region of low-momentum above them that is much thinner than that from a uniform wall. The r.m.s. in Fig. 13(d) confirm that these thin layers of relatively higher turbulence energy develop on the surface of the finlet rails, which are most probably responsible for the regions at high r.m.s. velocity observed in Fig. 9(d). These tiny layers of intense r.m.s. velocity cannot be captured well by the planar PIV of Fig. 10(d), presumably due to an averaging of the PIV measurement along the transversal direction.

From the maps in Fig. 13, velocity profiles can be calculated, which enables to directly quantify the effects of finlet rails on the flow behind the airfoil. For the case with finlet rails, two velocity profiles were determined, both obtained from conditional

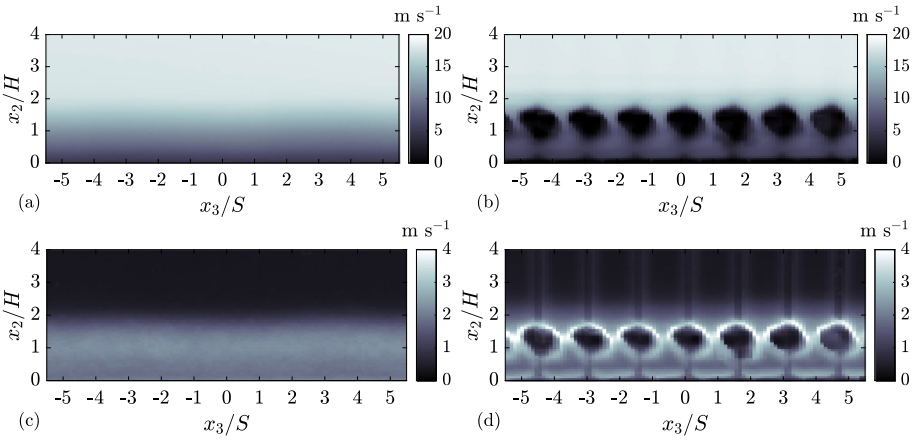

Fig. 12. Mean and r.m.s. streamwise velocity from stereoscopic PIV on a x_2x_3 plane passing through the trailing-edge of the airfoil model ($x_1 = 0$). (a,b) Mean streamwise velocity, $\overline{U_1}$, for (a) the baseline case and (b) the case with insert S2p5H4E5; (c,d) r.m.s. streamwise velocity, $U^{rms}{}_1$, for (c) the baseline case and (d) the case with insert S2p5H4E5.

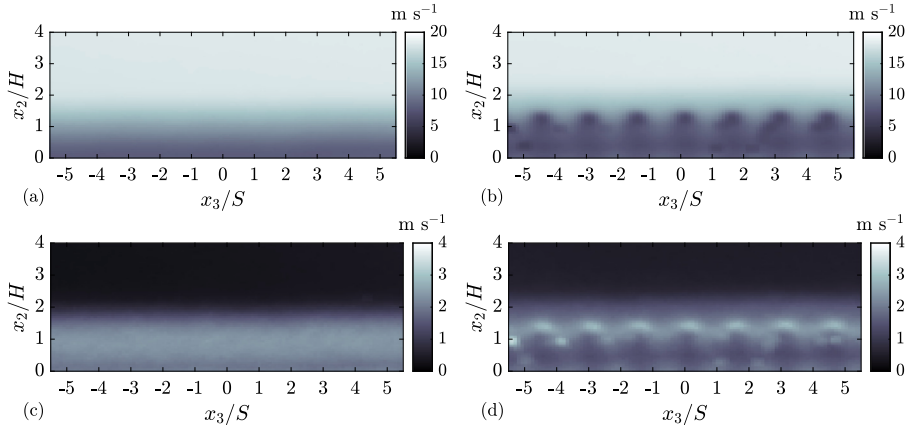

Fig. 13. Mean and r.m.s. streamwise velocity from stereoscopic PIV on a x_2x_3 plane at 5 mm distance from the trailing-edge of the airfoil model ($x_1 = 5$ mm $= 1E$). (a,b) Mean streamwise velocity, $\overline{U_1}$, for (a) the baseline case and (b) the case with insert S2p5H4E5; (c,d) r.m.s. streamwise velocity, $U^{rms}{}_1$, for (c) the baseline case and (d) the case with insert S2p5H4E5.

averaging. A velocity profile was calculated by averaging the velocities along lines of points behind the centers of the finlet rails, while another velocity profile was obtained from averaging the velocities along the lines at the intermediate positions between finlet rails. These velocity profiles are presented in Fig. 14, together with the profiles associated with the baseline case. In particular, Fig. 14(a) shows profiles of mean streamwise velocity and Fig. 14(b) shows profiles of r.m.s. streamwise velocity. For the mean velocity, the minimum in the graph from the rails wakes occurs slightly above the position of the finlets centers ($y/H = 1$), at $x_2/H \approx 1.2$. Up until this point, the streamwise velocity remains nearly constant and lower than $0.4U_1^{\infty}$, while beyond this point it grows abruptly. At wall-normal locations in the vicinity of the finlets centers, the profile in the rail wakes deviates significantly from the profile in the rail gaps. At $x_2/H \approx 1.7$, the differences between velocity profiles disappear, and for larger wall-normal locations the two lines tend to overlap. Profiles of r.m.s. velocity are presented in Fig. 14(b). Here it is very important to point out the strong attenuation of the energy content promoted in the region underneath the finlet rails. This can be observed when comparing the profiles from finlet case with the profile from the baseline case. If we then move to wall-normal positions above the finlet rails, the energy within the flow tends to increase, and it reaches the maximum at $x_2/H \approx 1.4$. Such energy increase is felt also in the gaps between rails although with lower intensity (line with red crosses). From comparing these r.m.s. values with those from the baseline case, we can observe how the finlet rails are overall effective in reducing the energy content close to the wall, but a penalty is paid at $x_2/H > 1.2$. These mean and r.m.s. velocity profiles are consistent with the velocity profiles obtained from finlet fences in previous experimental and numerical studies (see Afshari et al. [28], Shi and Lee [30], and Bodling and Sharma [29]). A phenomenon analogous to that described by [31] as a 'lift-up of energy carrying eddies' seems therefore to take place here, which increases the separation distance between source and scattering edge, and reduces the noise production efficiency [29]. The expression 'lift-up' evidences in this context a higher wall-normal position of the energetic turbulence structures when compared with the baseline

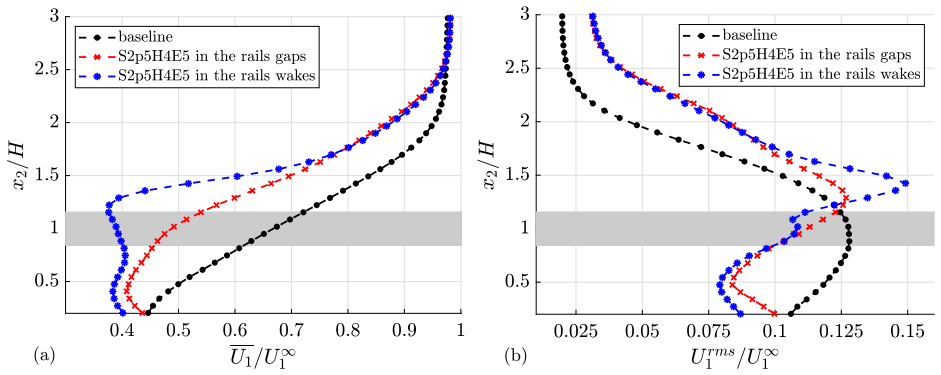

Fig. 14. (a) Mean and (b) r.m.s. profiles of streamwise velocity obtained from conditionally averaging velocity fields from stereoscopic PIV, on a x_2x_3 plane at 5 mm downstream from the trailing edge ($x_1 = 5$ mm $= 1E$). The gray regions mark the finlet rails.

case. Therefore, the expression should not induce to think that the energetic structures are characterized on average by a vertical velocity component that moves them away from the wall.

3.4. Physical mechanisms of noise reduction

According to Amiet's model [1] and to its extension by Roger & Moreau (2005) [48], the amplitude of the far-field trailing-edge noise is proportional *i.* to the wall pressure spectrum corresponding to the incident aerodynamic fluctuations, $\phi_{pp}(f)$, and *ii.* to the frequency-dependent spanwise (or transversal) pressure length scale, $\Lambda_z(f)$. In this section, we intend to investigate the effects of finlet rails on these physical quantities. Although the wall-pressure fluctuations in the proximity to the trailing edge cannot be directly measured with the present experimental set-up, the velocity fields from planar PIV can be used to estimate the so-called source term q, which is related to the wall-pressure fluctuations, p, through the Poisson equation [49,50]:

$$\nabla^2 p = q(x_1, x_2, x_3, t). \tag{3}$$

Following Kraichnan (1956) [50], the source term is

$$q(x_1, x_2, x_3, t) = -2\rho \frac{\mathrm{d}u_j}{\mathrm{d}x_i}\frac{\mathrm{d}\overline{U_i}}{\mathrm{d}x_j} - \rho \frac{\mathrm{d}^2}{\mathrm{d}x_i \mathrm{d}x_j}(u_i u_j - \overline{u_i u_j}). \tag{4}$$

From this equation, the source term is constituted by a first term referred as *T1*, which represents the interaction of turbulence with the mean shear, and a second term *T2*, which represents the turbulence-turbulence interaction. The relative contribution of the different terms constituting *T1* and *T2* is evaluated in the following, both from the baseline case and in presence of finlet rails. The analysis is performed on velocity fields from planar PIV from the 'TBL' field of view, after pre-processing these with a regression filter. At the trailing edge, the minimum spatial resolution of the PIV vector fields, intended as the size of the correlation windows, is of 2.9 times the Kolmogorov length scale, which is considered adequate to determine *T1* and *T2* [51–53]. The r.m.s. of the contributors to T1 and T2 are therefore assessed. The wall-normal distributions of the r.m.s. of four of the nine terms for T1 that can be calculated at the trailing edge from the 'TBL' field of view are presented in Fig. 15. As expected, the dominant contribution comes from $\frac{\mathrm{d}U_1}{\mathrm{d}x_2}\frac{\mathrm{d}u_2}{\mathrm{d}x_1}$, which includes the term corresponding to the mean shear of the flow $\frac{\mathrm{d}U_1}{\mathrm{d}x_2}$. The other three contributors are almost negligible. From comparing the baseline case (Fig. 15a), with the case with the insert (Fig. 15b), we can see that larger values of *T1* are reached for the baseline case. Therefore, the finlet rails are effective in attenuating *T1*. Moreover, because the airfoil surface is relatively distant from the field of view, it is expected that at $x_2/H \lessapprox 0.9$ the term grows even further, in that the term $\frac{\mathrm{d}U_1}{\mathrm{d}x_2}$ becomes stronger. In the case with finlets, larger values of $\frac{\mathrm{d}U_1}{\mathrm{d}x_2}\frac{\mathrm{d}u_2}{\mathrm{d}x_1}$ are reached relatively farther away from the wall when compared with the baseline case, which is consistent with having the TNTI shifted towards a higher wall-normal position. The value of the term grows rapidly when approaching the finlet wall, until it stabilizes a few millimeters above the finlet wall itself, which is represented by the gray region on the left side of the figure (see Fig. 16).

The distribution of $\frac{\mathrm{d}U_1}{\mathrm{d}x_2}\frac{\mathrm{d}u_2}{\mathrm{d}x_1}$ r.m.s. over the whole field of view can be seen in Fig. 17, for both cases. For the baseline case, much stronger values of $\frac{\mathrm{d}U_1}{\mathrm{d}x_2}\frac{\mathrm{d}u_2}{\mathrm{d}x_1}$ are reached when approaching the wall, as can be inferred when looking at the bottom left of Fig. 17(a). Overall, it appears evident from this figure that the application of finlet rails leads to a considerable mitigation of the r.m.s. of the dominant contributor to *T1* over the whole 'TBL' field of view. It is however worth highlighting that an estimate for this term in the region underneath the finlets is missing, and it cannot be obtained from the other PIV measurements of the present experimental set-up. However, the results from stereoscopic PIV show, as expected, that a low-momentum region exists underneath the finlet rails, which is also associated with low levels of turbulence (see Fig. 14(b)). We can therefore reasonably assume that *T1* is also attenuated in the region underneath the finlet rails when compared with the baseline case. After having quantified the mitigating effects of finlet rails on *T1*, it is of interest to explore the action of this surface treatment on *T2*.

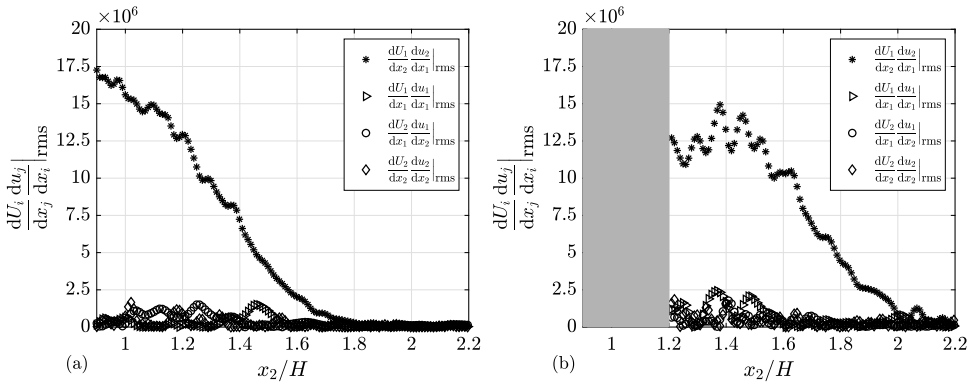

Fig. 15. R.m.s. of the *T1* contributors of the source term, q, computed at the trailing-edge of the airfoil model ($x_1 = 0$) as a function of the wall-normal positions for (a) the baseline case and (b) the case with insert S2p5H4E5.

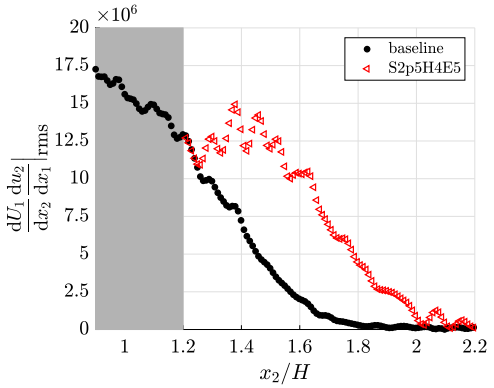

Fig. 16. R.m.s. of $\frac{dU_1}{dx_2}\frac{du_2}{dx_1}$ computed at the trailing-edge of the airfoil model ($x_1 = 0$) as a function of the wall-normal positions for the baseline case and the case with insert S2p5H4E5.

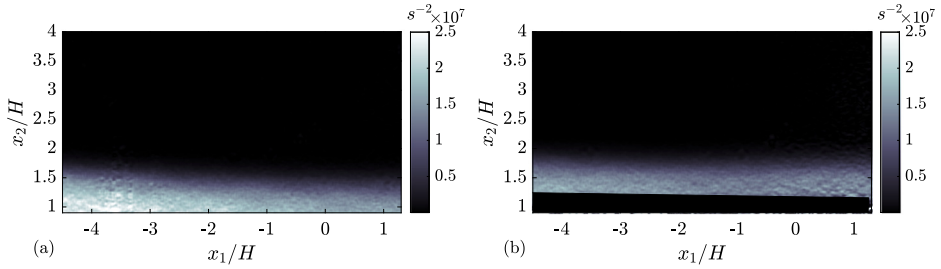

Fig. 17. R.m.s. of $\frac{dU_1}{dx_2}\frac{du_2}{dx_1}$ as a function of the streamwise and the wall-normal positions for (a) the baseline case and (b) the case with insert S2p5H4E5.

Similar to what previously shown for *T1*, Fig. 18 gives the r.m.s. values of the six contributors to *T2* that can be calculated from the 'TBL' field of view of planar PIV, at the trailing edge, and for varying wall-normal positions x_2/H. The contribution of the term $\rho\frac{d^2}{dx_i dx_j}\overline{u_i u_j}$ was found to be negligible and it was left out from presentation of the results. Again, a regression filter was applied to the velocity fields to attenuate the measurement noise in the PIV vector fields. The second-order derivatives, from which the terms contributing to *T2* are obtained, are more sensitive to noise than the first-order derivatives calculated for *T1*, therefore these results are expected to be affected by a relatively higher level of uncertainty compared with those for *T1*. From looking at Fig. 18, the dominant terms are in both cases $\frac{d^2u_1u_1}{dx_1^2}$ and $\frac{d^2u_1u_1}{dx_2^2}$, and similar trends can be observed for the baseline case and for the case with finlets. Specifically, all terms tend to monotonically increase their values when approaching the wall. It appears that larger values of the dominant terms are reached for the case with finlets. However, the field of view in Fig. 18(b) contains the surface of the finlet rails, beyond which the terms contributing to *T2* cannot be determined any more. For the baseline case, the wall of the model

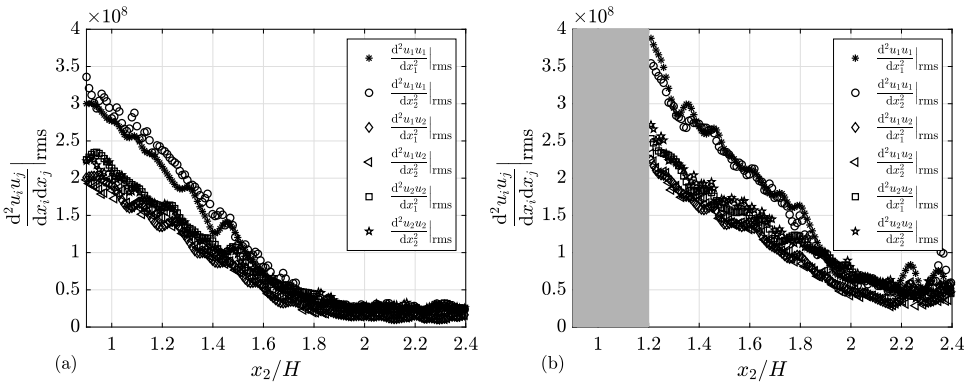

Fig. 18. R.m.s. of the *T2* contributors of the source term, q, computed at the trailing-edge of the airfoil model ($x_1 = 0$) as a function of the wall-normal position for (a) the baseline case and (b) the case with insert S2p5H4E5.

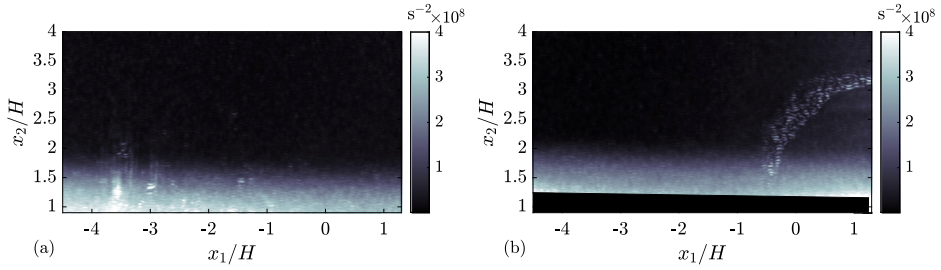

Fig. 19. R.m.s. of $\frac{d^2u_1u_1}{dx_2^2}$ as a function of the streamwise and the wall-normal position for (a) the baseline case and (b) the case with insert S2p5H4E5.

is at about $0.9H$ distance from the lower extreme of the field of view. It is expected that when the wall of the airfoil is approached, larger values are measured for the baseline case as opposed to the case with finlets. Similar to what was done previously, it is of interest to quantify the behavior of the dominant term $\frac{d^2u_1u_1}{dx_2^2}$ over the entire available field of view.

Fig. 19 shows the distribution of the r.m.s. of $\frac{d^2u_1u_1}{dx_2^2}$ throughout the entire 'TBL' field of view, both for the baseline case and for the case with finlet rails. Relatively broad regions characterized by large values of the dominant term are observed for the baseline case when moving towards the wall (bottom left), while analogous values can only be found on a small layer right above the surface of the finlet rails. From the results presented in Fig. 19 it is not possible to determine whether the finlet rails lead to a mitigation or to an increase of *T2*. At wall-normal position immediately above the finlet rails, the r.m.s. of *T2* is markedly larger than at the same position for the baseline case, while closer to model wall the opposite is expected to happen.

Direct quantification of $\frac{d^2u_1u_1}{dx_2^2}$ from stereoscopic PIV on the plane at 5 mm distance from the TE, i.e. at the edge of the finlet rails, can help to clarify the behavior of this term in the region underneath the surface treatment. The r.m.s. of $\frac{d^2u_1u_1}{dx_2^2}$ on the plane x_2x_3 is presented in Fig. 20. This quantification confirms what previously hypothesized. Immediately above the finlet rails ($x_2/H > 1.2$), the dominant contributor to *T2* exhibits larger values compared with the baseline case, consistent with Fig. 19. But, when moving to wall-normal positions closer to the wall, the r.m.s. of $\frac{d^2u_1u_1}{dx_2^2}$ drops significantly for the case with insert S2p5H4E5, whereas for the baseline case this term rises. Values much larger than those obtained above the finlet rails are reached for the baseline case at $x_2/H \approx 1$. However, the whole region $x_2/H \leq 1.2$ presents much higher values for the baseline case than for the case with insert.

The analysis presented until here evidences that the application of finlet rails determines an attenuation of the r.m.s. of *T1* and of *T2*, and, therefore, of the r.m.s. of the source term closer to the wall. The results were found to be robust to artificial modifications to the velocity vector fields meant to mimic the experimental uncertainty of PIV, although not presented here for brevity. The outcome of the analysis enables to infer that a mechanism of noise reduction for the finlet rails consists in attenuating the spectral content of the wall-pressure fluctuations, $\phi_{pp}(f)$. The observed attenuation of the wall-pressure fluctuations is expected to occur at low frequencies, which are those dominating when evaluating the r.m.s. of *T1* and *T2*, and also those at which the noise is reduced. The conclusion that finlet rails reduce the spectrum of the wall-pressure fluctuations would be consistent with what found in previous experimental studies on finlet fences, from wall-pressure measurements with flush-mounted microphones, particularly in Gstrein et al. [14,54]. In those measurements, the frequency range of noise reduction overlaps well with the frequency range of attenuation of the wall-pressure fluctuations, thus evidencing the prominent role played by the attenuation of the wall-pressure fluctuations in the aeroacoustic behavior.

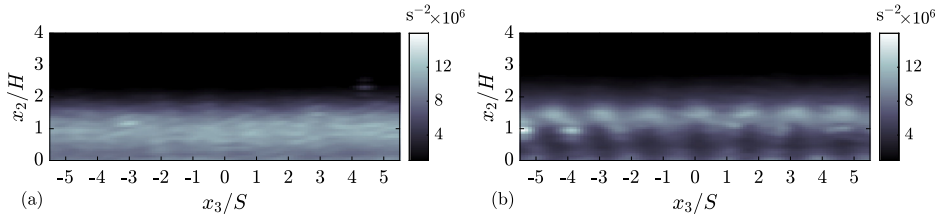

Fig. 20. R.m.s. of $\frac{\partial^2 u_1 u_1}{\partial x_3^2}$ from stereoscopic PIV on a x_2x_3 plane at 5 mm distance from the trailing-edge of the airfoil model, for (a) the baseline case and (b) the case with insert S2p5H4E5.

Another important consideration can be made when comparing the present results on finlet rails with the results from other studies on finlet fences. In finlet fences, a relatively low transversal spacing produces an increase in low-frequency noise [13,14,29], which can be associated with an increase of the wall-pressure fluctuations at an analogous frequency range (see figure 8 of Afshari et al. [28] and figure 9 of Gstrein et al. [14]). Finlet rails, on the other hand, seem to not present the same limitation. At the low frequencies, the treatment does not produce any noise increase (see Figs. 5 and 6), and the energetic wall-pressure fluctuations appear to be attenuated, as discussed in the previous paragraphs. The different finlet geometry leads therefore to a different aeroacoustic behavior, particularly at the low frequencies.

The lift-up of the energetic turbulence structures that we reported in the previous subsection can be considered responsible for the attenuation of the wall-pressure fluctuations. An analogous physical mechanism for noise reduction occurs also in active techniques of TBL-TE noise reduction, such as transverse jets injection and uniform blowing [55,56], where the injected air flow moves the energetic structures away from the wall, thus attenuating the wall-pressure fluctuations at the trailing edge.

We move now to discuss the effects of finlet rails on another physical quantity that is directly proportional to the estimated far-field noise according to Amiet's model, i.e. the spanwise (or transversal) pressure length scale, $\Lambda_z(f)$. Wall-pressure signals are not available from the present experimental set-up, therefore it is not possible to directly quantify $\Lambda_z(f)$. However, the characteristic transversal size of the energetic structures of turbulence can be estimated from the velocity fields obtained with stereoscopic PIV. To this aim, two-point correlation coefficients were calculated along lines parallel to wall, at four different wall-normal positions nearly equally spaced. The following relationship was applied to each snapshot

$$R(\Delta x_3) = \left. \frac{\overline{u_1(x_3)u_1(x_3+\Delta x_3)}}{\overline{u_1^2(x_3)}} \right|_{\text{line}} \tag{5}$$

where u_1 is the local fluctuation of the streamwise velocity, and the overline notation represents the ensemble average over the line points. The values of correlation as a function of the spanwise displacement were averaged among the different snapshots. The results are presented in Fig. 21. At the top row, two panels showing the mean streamwise velocity from stereoscopic PIV are presented, where horizontal lines of different colors indicate the points from which two-point correlation was calculated. Dots of different colors were placed at the origins of the Cartesian axes in the graphs of the correlation coefficients, in such a way to visually indicate the line of points from which the two-point correlation was computed. Four line plots of correlation coefficients as a function of the non-dimensional spanwise displacement along x_3, $\Delta x_3/H$, are presented in each of the four panels in Fig. 21(c,d,e,f). They were obtained from stereoscopic PIV velocity fields on a x_2x_3 plane passing through the trailing edge, called 'T.E.' in the legend, and on a x_2x_3 plane at 5 mm distance downstream from the trailing edge, called 'E5' in the legend, both for the baseline case and for the case with finlet rails. At each of the four wall-normal positions, the characteristic transversal length scale of the energy-containing turbulence structures can be compared by looking at the decaying rate of the correlation coefficients for increasing transversal displacement $\Delta x_3/S$. It can be observed that close to the wall, marked with a red dot, the smallest energetic structures are obtained for the case with finlet rails. Correlation coefficient associated with the other three cases tend to overlap for displacements $\Delta x_3/S < 0.5$. When looking at the wall-normal position immediately above, i.e. at the panel marked with a blue dot, the smallest energetic structures are obtained for the cases with finlet rails, for both the downstream locations under analysis. The same observation applies to the wall-normal position intersecting the finlet rails, marked with a black dot. However, it should be noted that for the case with finlet rails at the trailing edge, the correlation coefficients are calculated using velocity points that intersect the finlets. The largest wall-normal position, tagged with a cyan dot, is slightly above the treatment. Yet, the steepest decay of the correlation coefficients is obtained for the case with finlet rails at the trailing edge, while the other three cases nearly overlap. A peak in the correlation coefficients appears at $\Delta x_3/S = 1.5$ for most of the cases with surface treatments, independently of the wall-normal position. This should be attributed to the distance between the centers of adjacent rails corresponding to exactly 1.5 times the transversal spacing between the rails.

The analysis of the turbulent flow around the finlet rails concludes with a quantification of the convection velocities of the intense coherent structures of turbulence. A reduction of the convection velocities further weakens the scattering intensity, thus reducing the generation of noise [31]. Afshari et al. (2019) showed that finlets fences reduce the convection velocity of the turbulence structures, particular at intermediate to small scales, while the large scales appear to be less sensitive to it [28]. In the works of both Afshari et al. (2019) and Gstrein et al. (2022), the convection velocities of the turbulent eddies were estimated by determining the phase difference from microphone signals of wall-pressure fluctuations [14,28]. In the following, we adopted a different methodology, which is

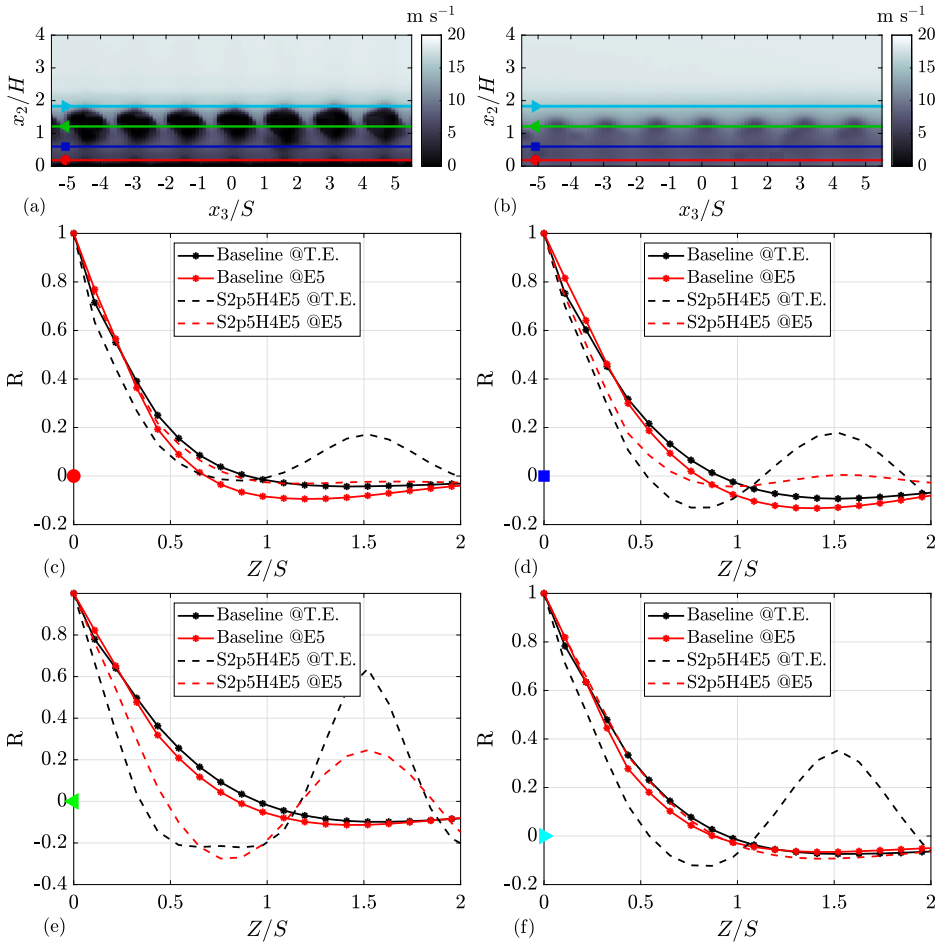

Fig. 21. Two-point correlation along lines parallel to the wall, obtained from streamwise velocity vector fields from stereoscopic PIV. (a,b) Mean streamwise velocity from stereoscopic PIV on (a) a x_1x_2 plane passing through the trailing-edge and (b) a x_1x_2 plane at 5 mm from the trailing-edge, where horizontal lines of different colors and symbols indicate the points used to calculate the two-point correlation. (c,d,e,f) Two-point correlation coefficients from points on the lines shown in (a) and (b), as a function of the non-dimensional lateral spacing x_3/S. Large symbols at the origins were added to visually indicate the line of points from which each panel was obtained. (For interpretation of the references to color in this figure legend, the reader is referred to the web version of this article.)

analogous to Fiscaletti, Ganapathisubramani & Elsinga (2015) [57]. Firstly, we identified the coherent structures of turbulence in the wake of the surface treatment using a criterion similar to that proposed by Zhou et al. (1999). This is based on the imaginary part of the eigenvalues of the reduced velocity gradient tensor, i.e. λ_{ci}. Secondly, we applied a threshold on the value of λ_{ci} with the aim of exclusively retaining the intense coherent structures. A coherent structure can be considered intense if λ_{ci} is locally larger than the product between a coefficient and the r.m.s. of λ_{ci} in points where λ_{ci} is non zero, as in the following relationship:

$$\lambda_{ci}(y,z) > C\lambda_{ci,rms} \tag{6}$$

where the value of C was chosen to be 2.5, although the results were found to be not particularly sensitive to variations of the coefficient C in the order of decimal. Finally, the streamwise velocities were determined in the centroids of the intense coherent structures, where the streamwise velocity of the centroid of the ith structure is identified as U_s^i. This methodology was applied to velocity vector fields from stereoscopic PIV on the plane at 5 mm distance from the TE, i.e. at the edge of the finlet rails. The range of wall-normal positions where the intense coherent structures were investigated was $0 < x_2/H < 2.5$. In Fig. 22, a sample of the baseline case from stereoscopic PIV on the plane at 5 mm distance from the TE shows the distribution of $\lambda_{ci}/\lambda_{ci,rms}$. Here, the described methodology is illustrated graphically, where black circles identify the intense structures of turbulence following the criterion of Eq. (6), and the dots inside them mark the centroids of these turbulence structures.

The probability density functions of the instantaneous streamwise velocities of the centroids of the intense coherent structures is presented in Fig. 23, both for the baseline case and for the case with insert S2p5H4E5. A clear reduction in the instantaneous streamwise velocities of the intense coherent structures can be appreciated, particularly for structures characterized by velocities

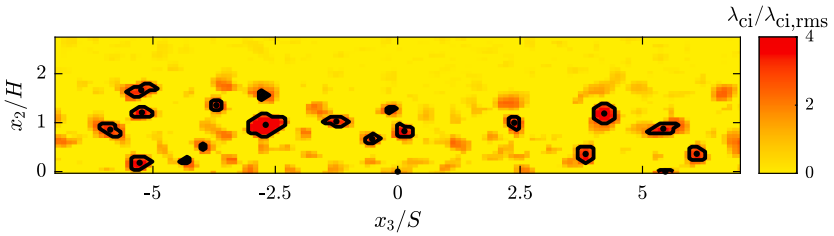

Fig. 22. A sample of the baseline case from stereoscopic PIV on the plane at 5 mm distance from the TE showing the distribution of $\lambda_{ci}/\lambda_{ci,rms}$. The dots represent the centroids of the identified structures (continuous black lines), where the local streamwise velocities, U_s^i, were estimated.

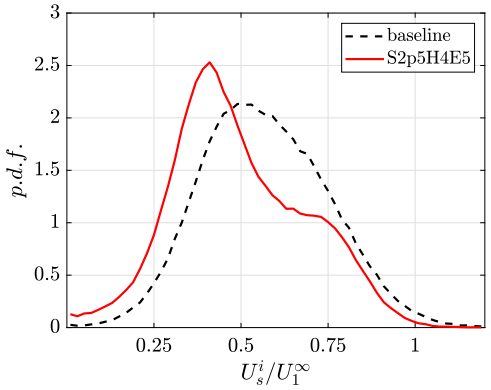

Fig. 23. Probability density functions of the instantaneous streamwise velocities of the centroids of the intense turbulence coherent structures, for the baseline case and the case with insert S2p5H4E5. The average values of instantaneous streamwise velocities of intense coherent structures are 11.4 m s^{-1} and 9.9 m s^{-1}, respectively for baseline case and for the case with insert.

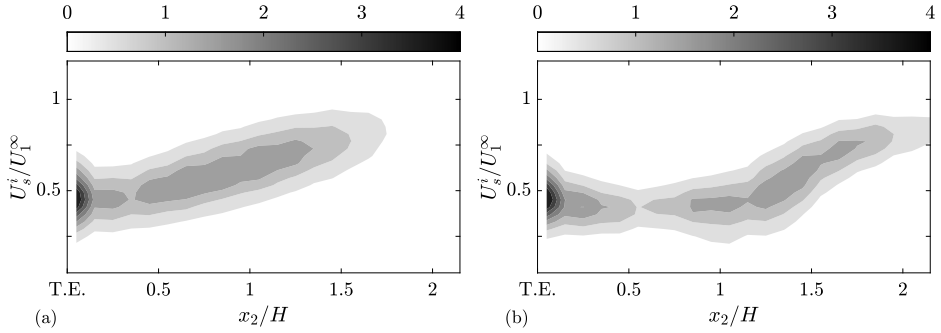

Fig. 24. Joint probability density functions between the position of the centroids of the intense turbulence coherent structures, on the x-axis, and their instantaneous streamwise velocities non-dimensionalized by the free-stream velocity, on the y-axis, for (a) the baseline case and (b) the case with insert S2p5H4E5.

lower than $0.75U_1^\infty$. For relatively larger velocities, i.e. $U_s^i/U_1^\infty > 0.75$, the two p.d.f.s tend to be similar to each other, and they nearly overlap. The average instantaneous streamwise velocities are reduced from 11.4 m s^{-1} for the baseline case to 9.9 m s^{-1} when applying the surface treatment. The relationship between the wall-normal position of the turbulence structures and the instantaneous streamwise velocities can be examined in a statistical sense when computing the joint p.d.f. of these quantities. Fig. 24 shows the results of this analysis. While the structures that are relatively close to the wall, i.e. in the region $x_2/H < 0.2$, do not appear to be particularly influenced by the treatment, the joint p.d.f. confirms that the turbulence structures are lifted-up. The region for the baseline case presenting high values of probability and shaped as an inclined ellipse (Fig. 24(a)) can also be identified for the

case with the insert too, although shifted towards higher wall-normal positions by approximately $0.5H$ (Fig. 24(b)). An additional evidence confirming the lift-up of turbulent structures is the lower probability of finding them in the range $0.3 < x_2/H < 0.7$ for the case with insert, as they have probably been shifted upwards. Another important observation is that the turbulence structures that, in the case with insert, are in the range $0.2 < x_2/H < 0.5$ have the same convection velocities as the turbulent structures at the wall, which suggests that the viscosity-dominated region extends to higher wall-normal positions here than for the baseline case.

4. Conclusions

Finlet rails were experimentally investigated as a strategy of TBL-TE noise reduction. Trailing-edge inserts with finlet rails of different geometries were 3D-printed and applied to a NACA $63_3 - 018$ airfoil model for 20% of the airfoil chord. The geometric parameters that were varied are the spacing between the rails, their height, and their downstream extension from the trailing-edge. Measurements of far-field noise and drag coefficient were conducted respectively with an array of microphones and through a wake-rake survey. It was found a maximum noise reduction of 4 dB at the Strouhal number based on the displacement thickness of $St_{\delta^*} = 0.093$, although at the penalty of increasing the high-frequency noise emission. The lowest transversal spacing among those under analysis, i.e. 2.5 mm, produced the maximum noise reduction. Such a transversal spacing is equivalent to δ^*, to $0.28\delta_{99}$, and to 0.6 the average position of the TNTI. An optimum in height of the rails was found from the present analysis to be of 4 mm, equivalent to $1.6\delta^*$, to $0.45\delta_{99}$, and to 0.9 the average position of the TNTI. Throughout the cases under analysis, the aeroacoustic performances were found to be sensitive to the increase of the angle of attack, with a decrease of the maximum noise reduction and an increase of the high-frequency penalty due to the boundary layer increase with respect to device. The drag coefficient for the configuration of maximum noise reduction presented an increase of 12.7% compared to the baseline case.

PIV measurements of the turbulent flow around the rails were conducted, both for the case showing the maximum noise reduction and for the baseline case. The treatment increases the wake span in the wall-normal direction by approximately $0.7H$, where H is the finlet height. Small regions at intense r.m.s. were found in the wake of the rails, which could be attributed to vortex shedding behind the rails. From measurements of the streamwise velocity in the plane along the wall-normal and transversal directions, the region underneath the finlet rails is characterized by a significant reduction of the turbulence energy compared with the baseline case. A region at relatively higher turbulence energy is, however, found above the finlet rails. This evidences that the energetic structures are 'lifted-up' and moved away from the scattering edge. The r.m.s. of the source term, related to the wall-pressure fluctuations through the Poisson equation, was estimated both for the case with finlet rails and for the baseline case. It was found that finlet rails attenuate the r.m.s. of the source term close to the wall, and therefore the spectral content of the wall pressure fluctuations at the low frequencies. The mitigation of the wall-pressure fluctuations as a consequence of the lift-up of the turbulence structures appears to be the mechanism for the reduction of the trailing-edge noise for finlet rails. An estimate of the spanwise extent of the energetic turbulence structures was obtained from two-point correlation along lines parallel to the wall, along the transversal direction. This relates to the spanwise pressure length scale entering Amiet's model for trailing-edge noise. In the region underneath the finlet rails, the transversal size of the energetic structures diminishes when the surface treatment is applied, while this effect vanishes right above the treatment itself. The combination of the lift-up of the turbulence structures, which reduces the wall-pressure fluctuations, with the smaller turbulence scales is responsible for the noise reduction observed for finlet rails.

CRediT authorship contribution statement

Daniele Fiscaletti: Conceptualization, Methodology, Investigation, Writing – original draft, Project administration, Funding acquisition. **Lourenco Tercio Lima Pereira:** Methodology, Investigation, Writing – review & editing. **Daniele Ragni:** Software, Resources, Writing – review & editing, Supervision.

Declaration of competing interest

Potential conflict of interest exists:

No conflict of interest exists.

We wish to confirm that there are no known conflicts of interest associated with this publication and there has been no significant financial support for this work that could have influenced its outcome.

Data availability

Data will be made available on request.

Acknowledgments

D.F. is funded by the Marie Skłodowska-Curie Actions of the European Union's Horizon 2020 Program under the Grant Agreement No. 895478 - ANACLETO.

References

[1] R.K. Amiet, Noise due to turbulent flow past a trailing edge, J. Sound Vib. 47 (1976) 387–393.
[2] R.K. Amiet, Effect of incident surface pressure field on noise due to turbulent flow past a trailing edge, J. Sound Vib. 57 (1978) 305–306.
[3] S. Oerlemans, P. Sijtsma, B. Méndez López, Location and quantification of noise sources on a wind turbine, J. Sound Vib. 299 (2007) 869–883.
[4] R. Snider, T. Samuels, B. Goldman, K. Brentner, Full-scale rotorcraft broadband noise prediction and its relevance to civil noise certification criteria, in: 69th Annual Forum of the American Helicopter Society, Vol. 2, Phoenix, Arizona, 2013, pp. 1293–1307.
[5] S. Li, S. Lee, Acoustic analysis and sound quality assessment of a quiet helicopter for air taxi operations, J. Am. Helicopter Soc. 67 (2022) 032001.
[6] M. Herr, W. Dobrzynski, Experimental investigation in low-noise trailing-edge design, AIAA J. 43 (6) (2005) 1167–1175.
[7] M. Gruber, P.M. Joseph, T.P. Chong, On the mechanisms of serrated airfoil trailing edge noise reduction, in: 17th AIAA/CEAS Aeroacoustics Conference, Vol. 2011–2781, Portland, Oregon, 2011.
[8] T. Chong, A. Vathylakis, P. Joseph, M. Gruber, Self-noise produced by an airfoil with nonflat plate trailing-edge serrations, AIAA J. 51 (11) (2013) 65–77.
[9] F. Avallone, W.C.P. van der Velden, D. Ragni, D. Casalino, Noise reduction mechanisms of sawtooth and combed-sawtooth trailing-edge serrations, J. Fluid Mech. 848 (2018) 560–591.
[10] S.A. Showkat Ali, M. Azarpeyvand, C.R.I. da Silva, Trailing-edge flow and noise control using porous treatments, J. Fluid Mech. 850 (2018) 83–119.
[11] A. Rubio-Carpio, R. Merino-Martínez, F. Avallone, D. Ragni, M. Sneller, S. van der Zwaag, Experimental characterization of the turbulent boundary layer over a porous trailing edge for noise abatement, J. Sound Vib. 443 (2019) 537–558.
[12] I.A. Clark, W.N. Alexander, W. Devenport, S. Glegg, J.W. Jaworski, C. Daly, N. Peake, Bioinspired trailing-edge noise control, AIAA J. 55 (3) (2017).
[13] A. Bodling, A. Sharma, Numerical investigation of noise reduction mechanisms in a bio-inspired airfoil, J. Sound Vib. 453 (2019) 314–327.
[14] F. Gstrein, B. Zang, Y.D. Mayer, M. Azarpeyvand, Airfoil trailing-edge noise reduction by application of finlets, AIAA J. 60 (1) (2022).
[15] V.B. Ananthan, R.A.D. Akkermans, T. Hu, P.Q. Liu, N. Rathje, Trailing-edge noise reduction potential of a locally applied shallow dimpled surface, J. Sound Vib. 525 (2022) 116745.
[16] S. Lee, L. Ayton, F. Bertagnolo, S. Moreau, T.P. Chong, P. Joseph, Turbulent boundary layer trailing-edge noise: Theory, computation, experiment, and application, Prog. Aerosp. Sci. 126 (100737) (2021).
[17] S. Li, S. Lee, Extensions and applications of lyu and ayton's serrated trailing-edge noise model to rotorcraft, in: 28th AIAA/CEAS Aeroacoustics Conference, Southampton, UK, 2022, pp. 2022–2916.
[18] M. Gruber, Airfoil Noise Reduction by Edge Treatments (Ph.D. thesis), University of Southampton, Southampton, 2011.
[19] B. Lyu, M. Azarpeyvand, S. Sinayoko, Prediction of noise from serrated trailing edges, J. Fluid Mech. 793 (2016) 556–588.
[20] S. Oerlemans, Reduction of wind turbine noise using blade trailing edge devices, in: 22nd AIAA/CEAS Aeroacoustics Conference, Lyon, France, 2016.
[21] E. Sarradj, T. Geyer, Noise generation by porous airfoils, in: 13th AIAA/CEAS Aeroacoustics Conference, Vol. 2007–3719, Rome, Italy, 2007.
[22] C. Teruna, F. Menegar, F. Avallone, D. Ragni, D. Casalino, T. Carolus, Noise reduction mechanisms of an open-cell metal-foam trailing edge, J. Fluid Mech. 898 (2020) A18.
[23] M. Herr, K.-S. Rossignol, J. Delfs, N. Lippitz, M. Mner, Specification of porous materials for low-noise trailing-edge applications, in: 20th AIAA/CEAS Aeroacoustics Conference, Atlanta, Georgia, 2014, pp. 2014–3041.
[24] S. Luesutthiviboon, D. Ragni, F. Avallone, M. Sneller, An alternative permeable topology design space for trailing-edge noise attenuation, Int. J. Aeroacoust. 20 (2021) 221–253.
[25] R.R. Graham, The silent flight of owls, J. R. Aero Soc. 38 (1934) 837–843.
[26] P. Zhou, S. Zhong, X. Zhang, On the effect of velvet structures on trailing edge noise: experimental investigation and theoretical analysis, J. Fluid Mech. 919 (2021) A11.
[27] I.A. Clark, C.A. Daly, W. Devenport, W.N. Alexander, N. Peake, J.W. Jaworski, S. Glegg, Bio-inspired canopies for the reduction of roughness noise, J. Sound Vib. 385 (2016) 33–54.
[28] A. Afshari, M. Azarpeyvand, A.A. Dehghan, M. Szőke, R. Maryami, Trailing-edge flow manipulation using streamwise finlets, J. Fluid Mech. 870 (2019) 617–650.
[29] A. Bodling, A. Sharma, Numerical investigation of low-noise airfoils inspired by the down coat of owls, Bioinspir. Biomim. 14 (2019) 016013.
[30] Y. Shi, S. Lee, Numerical study of 3-D finlets using Reynolds-averaged Navier–Stokes computational fluid dynamics for trailing edge noise reduction, Int. J. Aeroacoust. 19 (2020) 95–118.
[31] V.B. Ananthan, R.A.D. Akkermans, Trailing edge noise reduction using bio-inspired finlets, J. Sound Vib. 549 (2023) 117553.
[32] S. Luesutthiviboon, L.T. Lima Pereira, D. Ragni, F. Avallone, M. Sneller, Aeroacoustic benchmarking of trailing-edge noise from NACA 63_3-018 airfoil with trailing-edge serrations, AIAA J. 61 (1) (2023) 329–354.
[33] R.S. Ehrmann, E.B. White, Influence of 2D steps and distributed roughness on transition on a NACA 63_3-418, in: 32nd ASME Wind Energy Symposium, National Harbor, Maryland, 2014.
[34] E. Krog Kruse, N.N. Sørensen, C. Bak, A two-dimensional quantitative parametric investigation of simplified surface imperfections on the aerodynamic characteristics of a NACA 63_3-418 airfoil, Wind Energy 24 (2021) 310–322.
[35] R. Merino-Martínez, A. Rubio Carpio, L.T. Lima Pereira, S. van Herk, F. Avallone, D. Ragni, M. Kotsonis, Aeroacoustic design and characterization of the 3D-printed, open-jet, anechoic wind tunnel of Delft University of Technology, Appl. Acoust. 170 (2020) 107504.
[36] J.B. Barlow, W.H. Rae, A. Pope, Low-Speed Wind Tunnel Testing, John Wiley & Sons, 1999.
[37] E.L. Houghton, P.W. Carpenter, Aerodynamics for Engineering Students, Elsevier, 2003.
[38] G.P. Russo, Aerodynamic Measurements: From Physical Principles to Turnkey Instrumentation, Elsevier, 2011.
[39] H.H. Ku, Notes on the use of propagation of error formulas, J. Res. Natl. Bur. Stand. 70C (4) (1966).
[40] A. Kendall, M. Koochesfahani, A method for estimating wall friction in turbulent wall-bounded flows, Exp. Fluids 44 (2008) 773–780.
[41] R.J. Adrian, J. Westerweel, Particle Image Velocimetry, Cambridge University Press, 2011.
[42] F. Shan, A. Fujishiro, T. Tsuneyoshi, Y. Tsuji, Effects of flow field on the wall mass transfer rate behind a circular orifice in a round pipe, Int. J. Heat Mass Transfer 73 (2014) 542–550.
[43] A. Sciacchitano, Uncertainty quantification in particle image velocimetry, Meas. Sci. Technol. 30 (2019) 092001.
[44] J. Westerweel, C. Fukushima, J.M. Pedersen, J.C.R. Hunt, Momentum and scalar transport at the turbulent/non-turbulent interface of a jet, J. Fluid Mech. 631 (2009) 199–230.
[45] D.K. Bisset, J.C.R. Hunt, M.M. Rogers, The turbulent/non-turbulent interface bounding a far wake, J. Fluid Mech. 451 (2002) 383–410.
[46] K. Chauhan, J. Philip, C.M. de Silva, N. Huchins, I. Marusic, The turbulent/non-turbulent interface and entrainment in a boundary layer, J. Fluid Mech. 742 (2014) 119–151.
[47] A. Attili, J.C. Cristancho, F. Bisetti, Statistics of the turbulent/non-turbulent interface in a spatially developing mixing layer, J. Turbul. 15 (9) (2014) 555–568.
[48] M. Roger, S. Moreau, Back-scattering correction and further extensions of amiet's trailing-edge noise model. Part 1: theory, J. Sound Vib. 286 (2005) 477–506.
[49] O. Stalnov, P. Chaitanya, P.F. Joseph, Towards a non-empirical trailing edge noise prediction model, J. Sound Vib. 372 (2016) 50–68.
[50] R.H. Kraichnan, Pressure fluctuations in turbulent flow over a flat plate, J. Acoust. Soc. Am. 28 (3) (1956) 378–390.

[51] O.R.H. Buxton, S. Laizet, B. Ganapathisubramani, The effects of resolution and noise on kinematic features of fine-scale turbulence, Exp. Fluids 15 (2011) 1417–1437.
[52] N.A. Worth, T.B. Nickels, N. Swaminathan, A tomographic PIV resolution study based on homogeneous isotropic turbulence DNS data, Exp. Fluids 49 (3) (2010) 637–656.
[53] S. Tokgoz, G.E. Elsinga, R. Delfos, J. Westerweel, Spatial resolution and dissipation rate estimation in Taylor–Couette flow for tomographic PIV, Exp. Fluids 53 (2012) 561–583.
[54] F. Gstrein, B. Zang, M. Azarpeyvand, Application of finlets for trailing edge noise reduction of a NACA0012 airfoil, in: AIAA Aviation Forum, Vol. 2020–2502, Virtual Event, 2020.
[55] M. Szőke, D. Fiscaletti, M. Azarpeyvand, Effect of inclined transverse jets on trailing-edge noise generation, Phys. Fluids 30 (2018) 085110.
[56] M. Szőke, D. Fiscaletti, M. Azarpeyvand, Uniform flow injection into a turbulent boundary layer for trailing edge noise reduction, Phys. Fluids 32 (2020) 085104.
[57] D. Fiscaletti, B. Ganapathisubramani, G.E. Elsinga, Amplitude and frequency modulation of the small scales in a jet, J. Fluid Mech. 772 (2015) 756–783.